Investigating the effect of substrate thickness on the integrity of plasma sprayed hydroxyapatite coatings

BY

UNAISA DOCKRAT

Submitted in partial fulfilment of the requirements for the degree of

MASTERS (MSc) IN PHYSICS

In the Faculty of Natural and Agricultural Sciences

University of Pretoria

November 2022

Supervisor: Dr T.T. Thabethe

Co-Supervisor: Prof J.B. Malherbe

Co-Supervisor: Dr T.P. Ntsoane

DECLARATION

I, Unaisa Dockrat, declare that the thesis, which I hereby submit for the degree of MSc in Physics at the University of Pretoria, is my own work and has not been previously submitted by me for a degree at this or any other tertiary institution.

Signature:

Date : 25/11/2022

Summary

The demand for biomedical implants is on the rise for the maintenance and improvement of human health. These biomedical implants reinstate the function of living tissue and/or organs in the human body. Accidents, sports injuries as well as basic daily activities have caused the bone joints in the body to deteriorate at a fast pace. Thus, there has been an increase in the demand for more suitable and reliable ways to replace these joints and organs.

A biomaterial is any material of synthetic or natural origin that has the ability to repair or replace a function or a portion of the body in a secure, reliable, economic and physiologically acceptable manner to improve the quality of life. They may be categorized according to their relative tissue responses into bioinert, bioresorbable and bioactive. The bioactive materials, such as hydroxyapatite (HAp), upon contact with the human body, interacts with the environment and grows to become part of the component/environment. HAp is the second most thermodynamically stable and the least soluble of the calcium phosphates after fluorapatite (FAp).

HAp contains many mineral and chemical similarities with that of natural bone and therefore it has been widely studied for the use of biomedical application as bone implants. However, HAp contains weak mechanical properties such as brittleness. A metallic substrate, such as Ti-6Al-4V, with durable mechanical properties would therefore yield a desired result if the substrate were coated with HAp. The coated metallic substrate would contain the property to bond with the surrounding bone tissue and accelerate bone regeneration together with strong mechanical properties to withstand load-bearing applications.

This study was conducted by plasma spraying a HAp powder on Ti-6Al-4V substrates of different thicknesses. The effect of coating HAp on substrates with different thicknesses was investigated before and after immersing the sample in simulated bodily fluid. Immersion in simulated bodily fluid (SBF) was for various periods (7, 28 and 56 days). The structural changes, phase composition and stress before and after immersion were analysed using X-ray diffraction (XRD), Scanning Electron Microscopy (SEM) and Energy Dispersive X-ray Spectroscopy (EDS).

SEM was used to study the surface morphology of the surface of the substrates before and after immersion in the SBF. The as-sprayed samples for both substrate thicknesses appeared to have molten splats, various crystals and glassy regions on the surface indicating the surface was smooth. The 25 mm thick substrate (cylinder sample) had more cracks and crystals as compared to the 5 mm thick substrate (flat disk sample) which had more spherical particles. The surfaces after immersion for 7 days appear rougher and there was agglomeration of the crystals. A precipitate layer started forming on the surface after immersion for 28 days with a few voids present. After 56 days of immersion, the layer was observed to cover the full surface leaving no voids.

The results from the EDS were obtained before and after immersion in the SBF. Calcium and oxygen were the main elements present in both sample geometries. The flat disks had an increase in the calcium after 7 days of immersion and thereafter the calcium decreased with immersion time. The calcium in the cylinder substrates decreased from initial immersion. However, both sample geometries showed an increase of oxygen and a decrease of phosphorous after 56 days of immersion. Only the flat disks showed a presence of aluminium, chlorine and silicone after 56 days of immersion.

The results from the XRD analysis showed that the coating deposited on cylinder substrates had a greater intensity in the HAp peaks as compared to those on the flat disks. XRD quantitative phase analysis depicted, for both sample geometries, that HAp was the dominant phase with the thermal product CaO disappearing after 7 days of immersion. For the cylinder samples the HAp was observed to increase within 7 days of immersion and thereafter stabilized linearly with further immersion whereas for the flat disk sample it increased after 7 days of immersion and thereafter decreased gradually with immersion time. After 7 days of immersion the thermal products TCP and TTCP decreased for both geometries. The TTCP for the flat disks showed a small increase thereafter with immersion time while the TTCP for the cylinder substrates decreased with immersion time. The TCP for both geometries increases slightly after 28 days of immersion.

XRD residual stress investigation revealed a tensile stress state in the coatings deposited on both geometries. After air plasma spraying, the cylinder substrates had an average stress of 54.35 MPa which exceeded the ultimate tensile stress (UTS) of 38.0 – 48.0 MPa of the material. The average of the normal stresses thereafter decreased within 7 days of immersion to 51.38 MPa and thereafter continues to decrease with immersion time, eventually reaching an average stress of 35.57 MPa after 56 days. After air plasma spraying the flat disk, it had an average stress of 37.72 MPa. After immersion for 7 days, it increased to 40.10 MPa, reaching the UTS. It thereafter decreased with immersion time after 28 days and further decreased after 56 days of immersion to an average stress of 29.57 MPa. The shear components were found to be negligible not exceeding 12 MPa.

ACKNOWLEDGEMENTS

I would like to acknowledge the following people for their support and valuable contribution in the success of my study.

- My supervisor, Dr T.T. Thabethe for her endless guidance, support and discussion during the course of this study.
- My co-supervisor, Prof J.B Malherbe for his endless support and assistance.
- My co-supervisor, Dr T.P. Ntsoane, from NECSA for the assistance with the XRD measurements and data analysis as well as all his guidance.
- The head of department, Prof. C.C Theron, for his guidance and support.
- Mrs Charity Maepa, for her assistance with SEM and EDS.
- All the staff in the Physics department.
- My family, mostly my father- Hassen Dockrat, mother- Fharhana Dockrat, Ismail Dockrat, Muzaffar Dockrat, Bahiyya Areff Dockrat and Yusha Dockrat for all their prayers, endless support, love and encouragement.
- The financial assistance of the NRF is hereby acknowledged. Opinions expressed and conclusions arrived at, are those of the author and not necessarily attributed to the NRF.
- Most importantly the Almighty Allah for giving me all the power and strength to get to where I am.

Table of Contents

CHAPTER 1: INTRODUCTION 1

1.1 Background 1

1.2 Research Motivation 4

1.3 Research Aims & Objectives 5

1.4 Dissertation Outline 5

1.5 References 6

CHAPTER 2: MATERIALS 10

2.1 Hydroxyapatite 10

2.2 Ti-6Al-4V 13

2.3 References 16

CHAPTER 3: LITERATURE REVIEW 20

3.1 Literature Review 20

3.2 References 25

CHAPTER 4: REACTIONS AND INTERACTIONS 28

4.1 Thermodynamics 28

4.1.1 HAp Dehydroxylation 29

4.1.2 HAp Decomposition 30

4.2 Interactions with SBF 31

4.2.1 Simulated Bodily Fluid 32

4.2.2 Incubation in SBF 33

4.3 References 36

CHAPTER 5: EXPERIMENTAL PROCEDURE 40

5.1 Sample Preparation 40

5.2 Plasma-spraying deposition 41

5.3 Incubation experiment 44
5.4 X-ray Diffraction 47
5.4.1 Phase Identification 49
5.4.2 Residual Stress 50
5.4.2.1 Definition 50
5.4.2.2 Sources of residual stress 52
5.4.2.3 Residual stress in plasma sprayed coatings 53
5.4.2.4 Techniques for residual stress determination 54
5.5 Scanning Electron Microscopy 58
5.6 Energy Dispersive X-ray Spectroscopy 61
5.7 References 64
CHAPTER 6: RESULTS AND DISCUSSION 71
6.1 Cylinder Substrates 71
6.1.1 Scanning Electron Microscopy 71
6.1.2 Energy Dispersive X-ray Spectroscopy 73
6.1.3 X-ray Diffraction 75
6.1.3.1 Phase Identification 75
6.1.3.2 Residual Stress 79
6.2 Flat Disk Substrates 81
6.2.1 Scanning Electron Microscopy 81
6.2.2 Energy Dispersive X-ray Spectroscopy 83
6.2.3 X-ray Diffraction 85
6.2.3.1 Phase Identification 85
6.2.3.2 Residual Stress 88
6.3 Comparison 89

6.4 References 96

CHAPTER 7: CONCLUSION AND FUTURE WORK 97

7.1 Conclusion 97

7.2 Future work 100

Appendix A: Stress Results 101

ABBREVIATIONS

CTE	Coefficient of Thermal Expansion
CVD	Chemical Vapour Deposition
EDS	Energy Dispersive X-Ray Spectroscopy
FAp	Fluorapatite
HAp	Hydroxyapatite
NECSA	South African Nuclear Energy Corporation
OAP	Oxyapatite
OCP	Octacalcium Phosphate
OHAP	Oxyhydroxylapatite
QPA	Quantitative Phase Analysis
SBF	Simulated Bodily Fluid
c-SBF	conventional Simulated Bodily Fluid
i-SBF	ionized Simulated Bodily Fluid
m-SBF	modified Simulated Bodily Fluid
r-SBF	revised Simulated Bodily Fluid
s-SBF	synthetic Simulated Bodily Fluid
SEM	Scanning Electron Microscopy
TCP	Tricalcium Phosphate
TOPAS	Total Pattern Analysis Solution
TTCP	Tetracalcium Phosphate
UTS	Ultimate Tensile Stress
XRD	X-ray Diffraction

CHAPTER 1: INTRODUCTION

1.1 Background

Globally, there is an increase in the number of people that rely on biomedical implants for the maintenance or improvement of human health by reinstating the function of organs or living tissues in the body [1]. Over the years, bone disorder (Skeletal diseases) and heel diseases have been on the rise [2]. In some cases, the treatment for these diseases requires the use of biomedical implants in order to correct these defects [2]. Dental implants, bone replacements and load-bearing knee and hip endoprosthestic implants have been in large demand recently [2-3]. Endoprosthetic implants have seen an increase in demand due to knee and hip joints wearing away over the lifespan due to accidents and sports injuries. Reports indicate that the daily activities performed by humans can cause the deterioration of the joints to occur at a fast rate causing pain, inflammation and then leading to immobilization [2-5]. Thus, increasing the need for implants/biomedical devices over the years.

The advancement in biomedical implant technology (such as devices and systems) have through the years been noted to increase extensively [6-7]. Engineers and medical experts have enhanced the quality of the human life with medical devices and implants [6]. Even with these enhancements, there are still some draw backs in terms of long-term usage such as corrosion causing infection, nerve and tissue damage and coating delamination to mention a few. The development of these artificial devices requires careful evaluation. The device must be physically and biologically compatible with the host tissue. The device must also sustain the person till the end of time (long lifespan). However, the materials (biomaterials) used in these devices have some drawbacks. For instance, gold, cobalt and platinum appear to have an excessive elastic modulus, ceramics and carbon compounds were found to be very difficult to mould and metals and metal alloys are corrosive.

The biomaterial used in the devices are described as any materials of synthetic or natural origin. They have the ability to repair or replace a function or a portion of the body in a secure, reliable, economic and physiologically acceptable manner to improve the quality of life [1][8]. They are classified into bioinert, bioresorbable, and bioactive with each representing the relative tissue responses [9]. Bioinert materials only react minimally with the enclosing tissue once it comes in contact with the human body [9]. A material that disintegrates upon contact with the human body is known as a bioresorbable material [9]. The bioactive materials, upon contact with the human body, interacts with the environment (bone and tissue) and grows to become part of the component [9]. Since any artificial device/ implant comes into contact with the host tissue, it is of great importance that the implant is not rejected by the host. Hence, the implant needs to be nontoxic, compatible with the host tissue and able to connect with the host tissue.

Biomaterials consist of metals, ceramics, polymers and composites. In the past, biomaterials consisted of bronze and copper. The use of Cu and bronze was stopped because they caused Cu^{2+} to be released into the body which is poisonous [10-11]. Calcium sulphate and gold were then introduced in the applications of bone grafts and dentistry, respectively [12-13]. The calcium sulphate bone grafts were found to be an economic bone graft substitute however limitations such as donor morbidity and additional surgery were identified when using these bone grafts [14]. Gold has been used as a dental restorative material for years due to its functionality, biocompatibility, and aesthetics therefore it is known as the optimum material currently for dental restorations [15]. Alumina and zirconia were suggested to be used as biomaterials but were found to be inert [16]. Bio-glass and hydroxyapatite were then introduced and found to be biologically active materials [17].

Biomaterials can further be classified according to the specific host response into first, second and third generation [18]. The purpose of the first-generation biomaterials were to match the appropriate physical properties to the tissue that is required to be repaired or replaced, this category contains bio-inert materials [18]. Biomaterials that obtain the desired result and reaction are known as the second-generation biomaterials and consists of most bioactive materials [18]. Third-generation biomaterials consist of materials that are able to obtain a certain cellular response at the molecular level, this contains materials that fuse bioactive and bio-resorbable ideas to obtain the specific desired interaction [18]. Biomaterials have been used in the application of dental and bone implants [17], heart valves [17], breast implants [19], stents [20], hip replacements [17], spinal fusion [17] and to fill bone cavities [17].

Calcium phosphates have been used as a biomaterial from approximately a century ago [21]. A 'triple calcium phosphate' was used as a catalyst for bone growth and osteogenesis. However, Levitt [22] and Monroe [23] in approximately the 1960s developed a way to prepare calcium phosphate. This was proposed for use in prosthetics. The first use of calcium phosphate for dental applications was reported in 1974 in dogs [24-25]. However, in 1975 it was reported that porous calcium phosphate implants were used in surgery to create intrabony defects for dogs and the implants were found to be biocompatible and allowed for the growth into the bone. Then in the 1980s, dental procedures using thin films of hydroxyapatite began. This continued use spread and was then implemented in the use of orthopaedics and since then, the material has been investigated thoroughly for the use of biomedical applications.

There are approximately 13 calcium phosphates in the ternary system of $Ca(OH)_2H_3PO_4.H_2O$. Some examples of these compounds include; tricalcium phosphate, tetracalcium phosphate, amorphous calcium phosphate and hydroxyapatite [25]. Hydroxyapatite (HAp) is found in humans, animals as well as plants and mineral sources [26-27]. In this dissertation, HAp was used which contains a similar chemical composition to that of human bone.

However, HAp contains mechanical drawbacks hence a metal or metal alloy has been used in conjunction with HAp to withstand load-bearing applications. A Ti-alloy has been used in this investigation to improve the mechanical properties of HAp while combining the biocompatibility of HAp.

1.2 Research Motivation

Hydroxyapatite contains many mineral and chemical similarities with that of natural bone and therefore it has been widely studied for use in biomedical applications which consists of: load bearing and non-load bearing applications [28]. However, being a ceramic the major drawback of using HAp for load-bearing applications, is the weak mechanical properties such as its brittleness. Its low strength limits its bulk applications. HAp can therefore not be used alone for load-bearing applications. A metallic substrate with durable mechanical properties such as a Ti-alloy would therefore yield a desired result if coated with HAp, combining good bioconductivity with excellent mechanical properties of the substrate. The coated metallic substrate would contain the property to bond with the surrounding bone tissue and accelerate bone regeneration together with strong mechanical properties to withstand load-bearing applications [28]. Exemplary results of HAp fixated hip implants in patients were reported by Vedantam et al. [29]. No inflammation was observed. They also noted promotion of ingrowth of bone on the HAp surface.

Although thermal spraying of HAp on Ti alloy has been the preferred technique of choice at an industrial scale, other coating techniques have been used. Juliadmi et al. [30] coated Ti-6Al-4V with HAp using electrophoretic deposition (EPD). EPD was found to be an effective coating method producing thin HAp coatings of good quality. The thin coatings improved the osseointegration of the substrates. However Rad et al. [30] reported poor mechanical coatings generated by using EPD. These coatings were non-adhesive, non-uniform and had high porosity [30]. Kuroda et al. coated a Ti-alloy substrate with HAp by hydroprocessing [31]. However, osteoconductivity of the

coatings by hyroprocessing was not established. Air-plasma spraying has shown better results with regards to the durability and stability of the coatings on the metal surface as compared to other coating techniques [24]. A few studies [28-31] have been done to study the phase composition and crystallinity of the coatings on the top flat surface for various immersion periods on different substrates.

1.3 Research Aims and Objective

Aim

This study focuses on investigating the effect of substrate thickness on air-plasma sprayed coatings deposited on Ti-6Al-4V alloy substrates.

Objectives

This involves investigating the structural changes, phase composition and residual stress in HAp coatings deposited on the flat surface of the disk and the cylinder substrates before and after immersion in simulated bodily fluid for varying immersion times. This investigation will be carried out using X-ray diffraction (XRD), Scanning Electron Microscopy (SEM) and Energy Dispersive X-ray Spectroscopy (EDS).

1.4 Dissertation Outline

This dissertation is composed of seven chapters and is outlined as follows: Chapter 1 is the introduction which provides the background with the motivation of this study. Chapter 2 discusses the structure and properties of hydroxyapatite and Ti-6Al-4V. Chapter 3 is the literature review. Chapter 4 discusses thermodynamics and the reactions and interactions taking place, Chapter 5 is the experimental procedure. Chapter 6 is the experimental results and discussion. Chapter 7 presents the summary of results obtained and the future works planned.

1.5 References

[1] J. Park and R. S. Lakes, *Biomaterials*, 3rd ed. New York: Springer, p. 2, 2010.

[2] R. B. Heimann, "Thermal spraying of biomaterials", *Surface and Coatings Technology*, vol. 201, no. 5, pp. 2012-2019, 2006.

[3] H. M. Kremers, D. R. Larson, C. S. Crowson, W. K. Kremers, R. E. Washington, C. A. Steiner, W. A. Jiranek and D. J. Berry, "Prevalence of Total Hip and Knee Replacement in the United States", *The Journal of Bone and Joint Surgery-American Volume*, vol. 97, no. 17, pp. 1386-1397, 2015.

[4] T. Kim, C. W. See, X. Li and D. Zhu, "Orthopaedic implants and devices for bone fractures and defects: Past, present and perspective", *Engineered Regeneration*, vol. 1, pp. 6-18, 2020.

[5] D. J. Hunter and F. Eckstein, "Exercise and osteoarthritis", *Journal of Anatomy*, vol. 214, no. 2, pp. 197-207, 2009.

[6] Y. H. Joung, "Development of Implantable Medical Devices: From an Engineering Perspective", *International Neurourology Journal*, vol. 17, no. 3, p. 98, 2013.

[7] M. Zwawi, "Recent advances in bio-medical implants; mechanical properties, surface modifications and applications", *Engineering Research Express*, vol. 4, no. 3, p. 032003, 2022.

[8] M. Z. Rubežić, A. B. Krstić, H. Z. Stanković, R. B. Ljupković, M. Ranđelović S. and A. R. Zarubica, "Different Types Of Biomaterials: Structure And Application: A Short Review", 9th ed. Višegradska, 2020, pp. 69-79.

[9] G. Hennes and B. Ben-Nissan, "Biomaterials - Classifications and Behaviour of Different Types of Biomaterials", *AZoM.com*, 2004. [Online]. Available: https://www.azom.com/article.aspx?ArticleID=2630. [Accessed: 05- Dec- 2021].

[10] H. Tapiero, D. M. Townsend and K. D. Tew, "Trace elements in human physiology and pathology. Copper", *Biomedicine & Pharmacotherapy*, vol. 57, no. 9, pp. 386-398, 2003.

[11] E. Marin, F. Boschetto and G. Pezzotti, "Biomaterials and biocompatibility: An historical overview", *Journal of Biomedical Materials Research Part A*, vol. 108, no. 8, pp. 1617-1633, 2020.

[12] W. S. Pietrzak and R. Ronk, "Calcium Sulfate Bone Void Filler: A Review and a Look Ahead", *Journal of Craniofacial Surgery*, vol. 11, no. 4, pp. 327-333, 2000.

[13] H. Knosp, R. J. Holliday and C. W. Corti, "Gold in dentistry: Alloys, uses and performance", *Gold Bulletin*, vol. 36, no. 3, pp. 93-102, 2003.

[14] Y. Kumar C, N. K. B, J. Menon, D. K. Patro "Calcium Sulfate as Bone Graft Substitute in the Treatment of Osseous Bone Defects, A Prospective Study", *Journal Of Clinical And Diagnostic Research*, 2013.

[15] A. S. Sarthaj, A. Kumar and D. S. Majumder, "Comparative evaluation of wear resistance of cast gold with bulk-fill composites an in vitro study", *Journal of Conservative Dentistry*, vol. 21, no. 3, p. 302, 2018.

[16] C. Piconi and A. A. Porporati, "Bioinert Ceramics: Zirconia and Alumina", *Handbook of Bioceramics and Biocomposites*, pp. 59-89, 2016.

[17] L. L. Hench, "Bioceramics: From Concept to Clinic", *Journal of the American Ceramic Society*, vol. 74, no. 7, pp. 1487-1510, 1991.

[18] R. J. Narayan, "The next generation of biomaterial development", *Philosophical Transactions of the Royal Society A: Mathematical, Physical and Engineering Sciences*, vol. 368, no. 1917, pp. 1831-1837, 2010.

[19] M. Abdul-Al, A. Zaernia and F. Sefat, "Biomaterials for breast reconstruction: Promises, advances, and challenges", *Journal of Tissue Engineering and Regenerative Medicine*, vol. 14, no. 11, pp. 1549-1569, 2020.

[20] S. A. Sunny, A. Kishore, M. A. N. Manavalan and M. Ani, "Recent Trends In Biomaterials Used For Cardiovascular Stenting", *International Research Journal of Pharmacy*, vol. 4, no. 5, pp. 20-23, 2013.

[21] L. C. CHOW, "Next generation calcium phosphate-based biomaterials", *Dental Materials Journal*, vol. 28, no. 1, pp. 1-10, 2009.

[22] S. R. Levitt, P. H. Crayton, E. A. Monroe and R. A. Condrate, "Forming method for apatite prostheses", *Journal of Biomedical Materials Research*, vol. 3, no. 4, pp. 683-684, 1969.

[23] E. A. Monroe, W. Votava, D. B. Bass and J. McMullen, "New Calcium Phosphate Ceramic Material for Bone and Tooth Implants", *Journal of Dental Research*, vol. 50, no. 4, pp. 860-861, 1971.

[24] T. P. Ntsoane, "In-vitro investigation of air-plasma sprayed hydroxyapatite coatings deposited on two geometrically different substrates", PhD, University of Pretoria, 2020.

[25] S. V. Dorozhkin, *Calcium Orthophosphates in Nature, Biology and Medicine*. Singapore: Pan Stanford Pub., pp. 399-498,2009.

[26] N. A. S. Mohd Pu'ad, P. Koshy, H. Z. Abdullah, M. I. Idris and T. C. Lee, "Syntheses of hydroxyapatite from natural sources", *Heliyon*, vol. 5, no. 5, pp. e01588, 2019.

[27] V. S. Kattimani, S. Kondaka and K. P. Lingamaneni, "Hydroxyapatite–-Past, Present, and Future in Bone Regeneration", *Bone and Tissue Regeneration Insights*, vol. 7, 2016.

[28] R. Vedantam and C. Ruddlesdin, "The fully hydroxyapatite-coated total hip implant", *The Journal of Arthroplasty*, vol. 11, no. 5, pp. 534-542, 1996.

[29] D. Juliadmi, V. R. Fauzi, G. Gunawarman, H. Nur and M. H. Idris, "Hydroxyapatite Coating on Titanium Alloy Ti-6Al-4V with Electrophoretic Deposition (EPD) for Dental Root Application", *International Journal on Advanced Science, Engineering and Information Technology*, vol. 7, no. 6, p. 2152, 2017.

[31] K. Kuroda and M. Okido, "Hydroxyapatite Coating of Titanium Implants Using Hydroprocessing and Evaluation of Their Osteoconductivity", *Bioinorganic Chemistry and Applications*, vol. 2012, pp. 1-7, 2012.

CHAPTER 2: MATERIALS

2.1 Hydroxyapatite

Hydroxyapatite (HAp) with the formula $Ca_{10}(PO_4)_6(OH)_2$ is a calcium phosphate mineral belonging to a family of minerals called the apatites such as hydroxyapatite, fluorapatite and chlorapatite. HAp occurs naturally as a mineral and it can also be synthesized by the following commonly used methods: hydrothermal method, precipitation method, solvothermal method, spontaneous combustion method, bionic method and ultrasonic synthesis method [1]. It was discovered in the 1790s by Abraham Gottlob Werner however it was thought to be useless [1]. Bassett used X-ray diffraction thereafter in 1926 to observe human teeth and bone and found that the mineral component of bone and teeth was similar to that of hydroxyapatite [1]. The unit cell is hexagonal, and it consists of two molecules with the cell parameters of a = b = 9.432 Å and c = 6.881Å [2-3]. It can have a hexagonal structure or a monoclinic structure depending on the distribution of OH^- ions [4]. HAp with a monoclinic structure is only produced at very high temperatures and it has never been identified in calcified tissues. Therefore, the most commonly observed structure of HAp is the hexagonal structure with the $P6_3/m$ space group symmetry [2]. The structure is depicted in figure 2.1 and described by Mathew et al. [5].

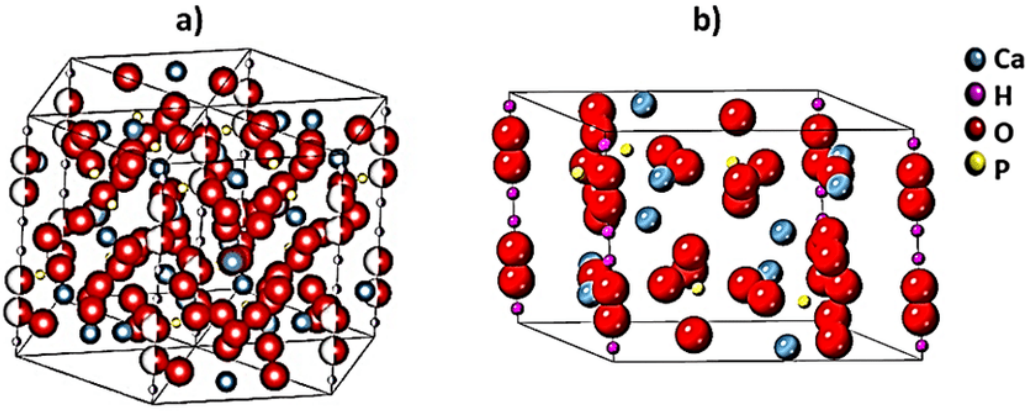

Figure 2.1: Figure displaying the (a) HAp unit cell and (b) HAp structure [6].

HAp is one of the most stable apatite's and it is also the least soluble apatite after fluorapatite [3]. It is also regarded as a bioactive material and this is due to the fact that it can enable bone formation without the need for fibrous tissue (regardless of how the HAp is obtained) [7]. Besides being bioactive, HAp is highly osteoconductive, non-toxic, non-immunogenic and has a crystal structure alike to that of mineral bone [3]. Its exceptional properties have made it one of the most investigated materials for medical implant application.

HAp has a stoichiometric Ca/P ratio of 1.67 which is comparable to the apatite found in human bones and teeth hence it is used in the application such as orthopedic and dental implants [8]. It was found that as the Ca/P ratio increases, the strength of HAp increases as a result eventually reaching a maximum value of approximately 1.67. The strength of HAp thereafter appears to decrease exponentially after reaching the value of 1.67 and the material appears porous as the Ca/P increases above 1.67 [3]. Table 2.1 shows a few properties of HAp [3].

Table 2.1: Table displaying properties of HAp [3].

Property	Value	
Thermal conductivity	0.013 W/(cm·K)	
Decomposition temperature	>1000 ℃	
Melting point	1614 ℃	
Tensile strength	38-300 MPa	For dense HAp
	~3 MPa	For porous HAp
Compressive strength	12-900 MPa	For dense HAp
	2-100 MPa	For porous HAp
Bending strength	38-250 MPa	For dense HAp
	2-11 MPa	For porous HAp
Young's (elastic) modulus	35-120 GPa	For dense HAp
Poisson's ratio	0.27	For synthetic HAp
Biocompatibility	High	
Bioactivity	High	
Biodegradation	Low	
Cellular compatibility	High	
Osteoconduction	High	
Ultimate Tensile Strength	38.0 – 48.0 MPa	

Hydroxyapatite (HAp) is used in the application of biomedical materials due to its excellent properties such as its osteoconductive and biocompatible properties. Specifically, it is used for tooth repairs, bone grafts [9], composite scaffolds for bone repair [10], bioactive coatings [11], drug delivery systems [12] and soft tissue regeneration [2]. Most recently, it has also been investigated for the use in bio-imaging and bio-labeling [13].

HAp has numerous advantages for the use of biomedical implants. The crystal structure of HAp is similar to that of natural bone hence allowing HAp to be a good candidate for bone grafts. It is documented that bioceramics made from HAp are simple to handle and easily adapts in case of defects occurring [14]. The HAp bioceramics is alike to the inorganic components of natural bone [14]. This mentioned activity is due to the surface of the bioceramic being osteoinductive or due to the release of Ca and P into the host tissue allowing the production of osteoblasts [14]. HAp allows the generation and enhances the adhesion of osteoblasts with the host-tissue [14].

The major drawback of using HAp for load-bearing applications, is the weak mechanical properties of HAp. The low strength of HAp limits the applications of HAp. HAp materials are not easily resorbable by the host tissue [2]. This has affected the application of HAp in bone implants and tissue engineering [2]. Bioceramics used for tissue engineering scaffolds made from HAp have been also observed to be brittle with a low flexibility and high stiffness [14].

2.2 Ti-6Al-4V

Titanium-6aluminium-4vanadium (Ti-6Al-4V) is a titanium alloy known as an α-β titanium alloy. It consists of Al being the α stabilizer which provides strength and V being the β stabilizer that decreases the phase-transformation temperature [15]. Ti-6Al-4V is manufactured mainly by additive manufacturing techniques (AM) such as directed energy deposition (DED), selective laser melting (SLM) and electron beam melting (EBM) [16]. The chemical composition of Ti-6Al-4V is outlined in table 2.2. This type of alloy exhibits excellent combination of properties compared to other titanium alloys. Ti-6Al-4V has a high mechanical strength together with high corrosion and temperature resistant properties [17]. The requirements for treating these type alloys are quite broad and extensive as compared to other titanium alloys which need very specific and demanding treatment methods [17]. Ti-6Al-4V is known to be extremely weldable and fairly moldable as compared to the other alloys [17-18]. The combination

of the properties of this type of alloy were found to be excellent by many researchers and a few of these properties are biocompatibility, ductility, high durability and fracture toughness, great strength, high producibility, light weight, low density and damage tolerance [16-18].

Table 2.2: Table showing the chemical composition of Ti-6Al-4V alloy [19].

Element	**Content (%)**
Titanium (Ti)	87.6 – 91
Aluminium (Al)	5.5 – 6.75
Vanadium (V)	3.5 – 4.5
Iron (Fe)	≤ 0.40
Oxygen (O)	≤ 0.20
Carbon (C)	≤ 0.080
Nitrogen (N)	≤ 0.050
Hydrogen (H)	≤ 0.015

This titanium alloy was initially produced in the 1950s for structural applications in aircrafts [16]. The use of Ti alloys in aircrafts has been widely accepted for many years [20]. Other industrial fields have found the use of Ti-6Al-4V quite advantageous to their specific applications. These fields include industries such as the seawater marine, chemical, automobile industries, missile components, spacecraft, hydrocarbon processing, power generation, nuclear waste control, metal ore extraction, naval components, armour plates, anodes, food processing, sporting equipment, pharmaceuticals, surgical equipment and biomedical implants [16][21].

Due to Ti-6Al-4V having excellent corrosion resistance, marine, ship building and chemical fields have reported it to be quite valuable [22]. The properties such as biocompatibility, strong mechanical strength, low density and high corrosion resistance are the reason why this specific alloy is used for the application in biomedical implants and bridges [23]. Titanium alloys have very strong mechanical properties and high corrosion and temperature resistant properties. Ti alloys have therefore gathered attention in the field for the use of biomedical implants and tissue replacements [23-24]. Due to its desirable properties, it has been investigated for the use in dental implants and artificial bones and joints [21][23]. Due to the harmonizing factor with the human body, Ti-6Al-4V has been found to be the best used titanium alloy in medicine as it is strong, non-toxic, biocompatible and long-lasting.

Ti-6Al-4V is quite useful in many industries however still containing some setbacks. Its low thermal conductivity and elastic modulus, high hardness, susceptibility to strain hardening and high chemical reactivity caused it to face many challenges in medical application and imposes restrains on its usage for biomedical implants [21][25]. When using Ti-6Al-4V conventionally, it is required to be forged, casted and machine cut, and this has resulted in some trouble observed with the resulting shape required for biomedical applications [26]. During the traditional manufacturing process, the Ti-6Al-4V has been found to have excessively high manufacturing costs and lengthy leading times together with an immense amount of wastes produced [26].

2.3 References

[1] G. Ma, "Three common preparation methods of hydroxyapatite", *IOP Conference Series: Materials Science and Engineering*, vol. 688, no. 3, p. 033057, 2019.

[2] K. Lin and J. Chang, "Structure and properties of hydroxyapatite for biomedical applications", 2022.

[3] N. Eliaz and N. Metoki, "Calcium Phosphate Bioceramics: A Review of Their History, Structure, Properties, Coating Technologies and Biomedical Applications", *Materials*, vol. 10, no. 4, p. 334, 2017.

[4] E. Fiume, G. Magnaterra, A. Rahdar, E. Verné and F. Baino, "Hydroxyapatite for Biomedical Applications: A Short Overview", *Ceramics*, vol. 4, no. 4, pp. 542-563, 2021.

[5] M. Mathew and S. Takagi, "Structures of biological minerals in dental research", *Journal of Research of the National Institute of Standards and Technology*, vol. 106, no. 6, p. 1035, 2001.

[6] M. Rabiei, A. Palevicius, A. Dashty, S. Nasiri, A. Monshi, A. Doustmohammadi, A. Vilkauskas and G. Janušas, "X-ray Diffraction Analysis and Williamson-Hall Method in USDM Model for Estimating More Accurate Values of Stress-Strain of Unit Cell and Super Cells (2 × 2 × 2) of Hydroxyapatite, Confirmed by Ultrasonic Pulse-Echo Test", *Materials*, vol. 14, no. 11, p. 2949, 2021.

[7] Y. Y. Chung, S. C. Ki, K. Y. So, D. H. Kim, K. H. Park and Y. S. Lee, "High revision rate of hydroxyapatite-coated ABG-I prosthesis", *Journal of Orthopaedic Science*, vol. 14, no. 5, pp. 543-547, 2009.

[8] A. Bhattacharjee, Y. Fang, T. J. N. Hooper, N. L. Kelly, D. Gupta, K. Balani, I. Manna, T. Baikie, P. T. Bishop, T. J. White and J. V. Hanna, "Crystal Chemistry and Antibacterial Properties of Cupriferous Hydroxyapatite", *Materials*, vol. 12, no. 11, p. 1814, 2019.

[9] L. Xia, K. Lin, X. Jiang, Y. Xu, M. Zhang, J. Chang and Z. Zang, "Enhanced osteogenesis through nano-structured surface design of macroporous hydroxyapatite bioceramic scaffolds via activation of ERK and p38 MAPK signaling pathways", *Journal of Materials Chemistry B*, vol. 1, no. 40, p. 5403, 2013.

[10] S. Xu, J. Liu, L. Zhang, F. Yang, P. Tang and D. Wu, "Effects of HAp and TCP in constructing tissue engineering scaffolds for bone repair", *Journal of Materials Chemistry B*, vol. 5, no. 30, pp. 6110-6118, 2017.

[11] O. Gherasim, A. M. Grumezescu, V. Grumezescu, I. Negut, M. F. Dumitrescu, M. S. Stan, I. C. Nica, A. M. Holban, G. Socol and E. Andronescu, "Bioactive Coatings Based on Hydroxyapatite, Kanamycin, and Growth Factor for Biofilm Modulation", *Antibiotics*, vol. 10, no. 2, p. 160, 2021.

[12] Y. Wen, J. Li, H. Lin, H. Huang, K. Song, K. Duan, T. Guo and J. Weng, "Improvement of Drug-Loading Properties of Hydroxyapatite Particles Using Triethylamine as a Capping Agent: A Novel Approach", *Crystals*, vol. 11, no. 6, p. 703, 2021.

[13] K. Deshmukh, M. M. Shaik, S. R. Ramanan and M. Kowshik, "Self-Activated Fluorescent Hydroxyapatite Nanoparticles: A Promising Agent for Bioimaging and Biolabeling", *ACS Biomaterials Science & Engineering*, vol. 2, no. 8, pp. 1257-1264, 2016.

[14] H. S. Lee, S. H. Byun, S. W. Cho and B. E. Yang, "Past, Present, and Future of Regeneration Therapy in Oral and Periodontal Tissue: A Review", *Applied Sciences*, vol. 9, no. 6, p. 1046, 2019.

[15] L. Xue, "Laser consolidation: a rapid manufacturing process for making net-shape functional components", *Advances in Laser Materials Processing*, pp. 492-534, 2010.

[16] S. Liu and Y. C. Shin, "Additive manufacturing of Ti6Al4V alloy: A review", *Materials & Design*, vol. 164, p. 107552, 2019.

[17] R. R, Boyer, "Titanium for aerospace: Rationale and applications", *Advanced Performance Materials*, vol. 2, no. 4, pp. 349-368, 1995.

[18] R. R. Boyer, "Titanium and Its Alloys: Metallurgy, Heat Treatment and Alloy Characteristics", *Encyclopedia of Aerospace Engineering*, 2010.

[19] "Grade 5 Ti-6Al-4V Alloy (UNS R56200)", *AZoM.com*, 2013. [Online]. Available: https://www.azom.com/article.aspx?ArticleID=9299. [Accessed: 06- May- 2022].

[20] I. Inagaki, T. Takechi, Y. Shirai and N. Ariyasu, "application and features of titanium for the aerospace industry", Osaka, 2014.

[21] A. Saini, B. Pabla and S. Dhami, "Developments in cutting tool technology in improving machinability of Ti6Al4V alloy: A review", *Proceedings of the Institution of Mechanical Engineers,* Part B: Journal of Engineering Manufacture, vol. 230, no. 11, pp. 1977-1989, 2016.

[22] A. S. Oryshchenko, I. V. Gorynin, V. P. Leonov, A. S. Kudryavtsev, V. Mikhailov and E. V. Chudakov, "Marine titanium alloys: Present and future", *Inorganic Materials: Applied Research*, vol. 6, no. 6, pp. 571-579, 2015.

[23] C. Cui, B. Hu, L. Zhao and S. Liu, "Titanium alloy production technology, market prospects and industry development", *Materials & Design*, vol. 32, no. 3, pp. 1684-1691, 2011.

[24] Y. Murakami, Preview View on ScienceDirect Metal Fatigue: Effects of Small Defects and Nonmetallic Inclusions, 2nd ed. Burlington: *Elsevier*, pp. 293-316, 2019.

[25] R. K. Gupta, V. A. Kumar, C. Mathew and G. S. Rao, "Strain hardening of Titanium alloy Ti6Al4V sheets with prior heat treatment and cold working", 2016.

[26] R. Huang, M. Riddle, D. Graziano, J. Warren, S. Das, S. Nimbalkar, J. Cresko and E. Masaneta, "Energy and emissions saving potential of additive manufacturing: the case of lightweight aircraft components", *Journal of Cleaner Production*, vol. 135, pp. 1559-1570, 2016.

CHAPTER 3: LITERATURE REVIEW

3.1 Literature Review

There is an increase in the number of patients that rely on biomedical implants. A biomedical implant is a synthetic material that is made to be used in the human body to reinstate the function of a missing biological structure, maintain a flawed biological structure, or improve a current biological structure [1-4]. The market for biomedical implants is expected to grow at a cumulative growth rate (CAGR) of 7.2% from 2020 to 2027 [5]. Development of these implants is planned to ensure that the supposed material contains improved properties such as mechanical strength, biological activity and compatibility, and chemical durability [6]. This material is designed to carry out certain needs in the human body thus having an intricate variation of properties [6].

Many studies have been done to develop different types of biomaterials using various metal substrates. However, investigations have shown that the metal substrates have had some negative biological aspects. Upon contact with the host, there is adhesion of proteins on the substrate due to electrostatic interactions [7]. The substrates used for the implants have also been found to cause infection at the surgery site due to a low antibacterial response of the metal [7].

Titanium (Ti) substrates and its alloys have been selected and researched extensively for the use of biomedical implants. Examples include dental implants, orthopaedic implants, screws for bone fractures and hip and knee replacements [8-9]. These titanium alloy substrates were found to be more effective for implants since the behaviour of these substrates in the host have produced a much better response than other metal substrates [7]. Ti alloys have also been found to have a greater biocompatibility, lower Young's modulus and a much higher corrosion resistance as compared to other metal biomaterials [10].

However, the major flaw encountered with the Ti alloys is the osseointegration of the implants in the host. It would take a long time for the Ti alloy to be fixed to the bone to be stable enough hence the osteoconductivity of these implants are required to be enhanced. The implants therefore had to be modified in a way that they do no harm upon contact with the host. Methods to modify the surface have been researched such as: (1) surface treatments and (2) coating the surface with a bioactive/biocompatible compound [11]. Surface treatment was then established and found to decrease the adsorption of proteins on the substrate surface [12]. It has however been reported that surface treatments were not sufficient enough to attain the level of osteoconductivity needed [10].

Modifying the surface of the Ti implants by coating the surface with a biocompatible material would therefore solve the problem of osteoconductivity. The biocompatible coatings however have caused a major drawback since the adhesion strength between the substrate and coating is restricted by certain factors such as irregular coating thickness, weak interfacial bonding and splitting of the coating due to residual stress [6][10]. Hydroxyapatite however has been widely studied for the use in biomedical implants and has been reported to be one of the most biocompatible materials. The material has a composition and structure very much alike to that of the human bone hence allowing osseointegration with the human body. Hydroxyapatite is very bioactive however it contains weak mechanical properties which would restrict its load-bearing applications. Thus, it was found that using a metal with good mechanical properties coated with HAp would increase the strength of the HAp without reducing its biocompatibility [6]. There have been various coating techniques reported to coat the HAp on the metal substrate. Some of these techniques are briefly summarised in table 3.1.

Table 3.1: Table displaying different techniques for HAp coatings [6][8].

Technique	Thickness	Advantages	Disadvantages
Plasma spraying	>20 µm	Inexpensive, high deposition rate & low coating degradation.	High processing temperature, weak adhesion & non-uniform coating density.
Sol-gel	<1µm	Coat complex shapes, low processing temperature, cheap & pure coating.	Weak adhesion & requires controlled atmosphere at some stages.
Dip coating	0.05-0.5 mm	Cheap, high deposition rate & can coat complex shapes.	High processing temperature & mismatch of thermal expansion.
Electrophoretic deposition	100-2000 µm	Coat complex shapes, high deposition rate & uniform coating thickness	High processing temperature & difficult to produce crack-free coating.
Electrochemical deposition	50-500 µm	High deposition rate, cheap, uniform coating thickness & can coat complex shapes.	Weak adhesion.
Sputter coating	0.02-1 µm	Uniform coating thickness on flat surface.	Expensive, low deposition rate, produces amorphous coatings & no coating on complex shapes.
Pulsed laser deposition	0.05-5 µm	Uniform coating thickness on flat surface.	Expensive, low deposition rate, produces amorphous coatings & no coating on complex shapes.
Biomimetic deposition	<30 µm	Low processing temperature, can coat complex shapes & coating forms bone-like apatite.	Low deposition rate & coating contains low degree of crystallinity.

From the above-mentioned techniques, plasma spraying has been the most extensively used and investigated for depositing HAp on Ti alloys. Plasma spraying is also the only technique authorized for depositing coatings on materials used for bio-implants by the Food and Drug Administration (FDA), USA [13]. Plasma spraying has an excellent deposition rate and produces a coating with more uniform thickness and a higher density; thus, it has been clinically approved [13]. Gao et al. [14] has researched the effect on the bioactivity and corrosion resistance of Mg alloys after being plasma-sprayed with HAp and immersed in SBF. It was found that the HAp coating deposited via plasma spray technique, had increased the performance of the bioactivity and corrosion resistance of the metal alloy [14].

A study was done by Priyadarshini et al. [15] by depositing HAp incorporated with cerium on Ti-6Al-4V to improve the corrosion resistance and bioactivity. The Ce-HAp coating was deposited on the alloy using spin coating techniques and thereafter immersed in simulated bodily fluid for 10 and 20 days [15]. The bioactivity increased and the strength of the adhesion between substrate and coating appeared to increase [15]. Sobolev et al. [16] investigated the effect of osseointegration with human bone by developing a HAp coating on a Ti alloy surface using plasma electrolytic oxidation (PEO) treatment and immersing the substrates in SBF. It was found that the HAp coating grew after exposed to the SBF and there was a high level of osseointegration created [16]. Liu et al. [17] studied the performance of growing osteoblast cells on the surface of HAp coated titanium in order to enhance the stability of the HAp coating on titanium for bone implants and bone tissue engineering. It was reported that the HAp improved the biocompatibility of the titanium surface [17].

Sol-gel technique for coating titanium alloys with HAp has been studied by Jaafar et al. [18]. HAp was coated on the titanium substrate using sol-gel process. It was found that the biocompatibility and adhesion increased on the Ti substrate and the corrosion resistance was enhanced [18]. There were however drawbacks observed when coating the substrate with HAp using the sol-gel technique. Some unknown parameters need to

be investigated using the sol-gel method as this would improve the performance of the HAp coating [18].

Coating Ti substrates by plasma spraying with HAp and β-TCP for the use of biomedical implants was investigated by Pillai et al. [19]. It was found that by choosing a particular composition of powder to plasma spray, this would allow for coatings with adjustable solubility for the use of orthopaedic application [19]. Singh et al. [20] similarly tried to investigate the result of plasma spraying HAp and HAp-silicon dioxide (SiO_2) on AISI 304 for the use of biomedical implants. They observed that the substrate coated with HAp-silicon oxide showed more resistance to corrosion as compared to the HAp coated substrate [20]. However, the HAp coated substrate showed more resistance to corrosion as compared to the uncoated substrate [20]. It was observed by various researchers that the coatings formed on the substrates by plasma spraying had the ability to be bioactive, dense and were quite strongly bonded to the substrate [21].

Although HAp coatings deposited on Ti alloy substrates have been extensively investigated over the years [6-21], to our knowledge no study has been done to investigate the effect of titanium alloy thickness on plasma-sprayed coatings. The aim of this study is to investigate the effect of substrate thickness on HAp coatings deposited by air plasma spraying on Ti-6Al-4V alloy substrates. This study focuses on the quality and biological behaviour of HAp coatings, by investigating the structural changes, phase composition and stress of air-plasma sprayed HAp coatings deposited on the flat disk and the cylinder substrates of as sprayed and samples immersed in simulated bodily fluid for varying immersion times. The observed results will be explained from the heat transfer point of view.

3.2 References

[1] R. Balint, N. Cassidy and S. Cartmell, "Conductive polymers: Towards a smart biomaterial for tissue engineering", *Acta Biomaterialia*, vol. 10, no. 6, pp. 2341-2353, 2014.

[2] A. Hasan et al., "Electrospun scaffolds for tissue engineering of vascular grafts", *Acta Biomaterialia*, vol. 10, no. 1, pp. 11-25, 2014.

[3] M. Valente, D. de Castro, A. Macedo, A. Shimano and A. dos Reis, "Comparative analysis of stress in a new proposal of dental implants", *Materials Science and Engineering: C*, vol. 77, pp. 360-365, 2017.

[4] Y. Qin, "Textiles for implants and regenerative medicine", *Medical Textile Materials*, pp. 133-143, 2016.

[5] "Medical Implants Market Size | Industry Forecast by 2027", *Allied Market Research*, 2022. [Online]. Available: https://www.alliedmarketresearch.com/medical-implants-market#:~:text=The%20global%20medical%20implants%20market,7.2%25%20from%202020%20to%202027. [Accessed: 07 Mar 2022].

[6] P. Choudhury and D. Agrawal, "Hydroxyapatite (HA) coatings for biomaterials", *Nanomedicine*, pp. 84-127, 2012.

[7] V. Mantripragada, B. Lecka-Czernik, N. Ebraheim and A. Jayasuriya, "An overview of recent advances in designing orthopedic and craniofacial implants", *Journal of Biomedical Materials Research Part A*, 2012.

[8] V. Huynh, N. Ngo and T. Golden, "Surface Activation and Pretreatments for Biocompatible Metals and Alloys Used in Biomedical Applications", *International Journal of Biomaterials*, vol. 2019, pp. 1-21, 2019.

[9] D. de Andrade et al., "Titanium–35niobium alloy as a potential material for biomedical implants: In vitro study", *Materials Science and Engineering: C*, vol. 56, pp. 538-544, 2015.

[10] T. Hacioglu, Z. Evis, A. Tezcaner and M. Aydınol, "Effects of surface pretreatments and coating period on hydroxyapatite coating of Ti6Al4V alloy", *Journal of the Australian Ceramic Society*, vol. 56, no. 2, pp. 545-557, 2019.

[11] K. Kuroda and M. Okido, "Hydroxyapatite Coating of Titanium Implants Using Hydroprocessing and Evaluation of Their Osteoconductivity", *Bioinorganic Chemistry and Applications*, vol. 2012, pp. 1-7, 2012.

[12] F. Poncin-Epaillard et al., "Surface Treatment of Polymeric Materials Controlling the Adhesion of Biomolecules", *Journal of Functional Biomaterials*, vol. 3, no. 3, pp. 528-543, 2012.

[13] A. Singh, G. Singh and V. Chawla, "Mechanical properties of vacuum plasma sprayed reinforced hydroxyapatite coatings on Ti-6Al-4V alloy", *Journal of the Australian Ceramic Society*, vol. 53, no. 2, pp. 795-810, 2017.

[14] Y. Gao, Y. Liu and X. Song, "Plasma-Sprayed Hydroxyapatite Coating for Improved Corrosion Resistance and Bioactivity of Magnesium Alloy", *Journal of Thermal Spray Technology*, vol. 27, no. 8, pp. 1381-1387, 2018.

[15] B. Priyadarshini, S. Ramya, E. Shinyjoy, L. Kavitha, D. Gopi and U. Vijayalakshmi, "Structural, morphological and biological evaluations of cerium incorporated hydroxyapatite sol–gel coatings on Ti–6Al–4V for orthopaedic applications", *Journal of Materials Research and Technology*, vol. 12, pp. 1319-1338, 2021.

[16] A. Sobolev, A. Valkov, A. Kossenko, I. Wolicki, M. Zinigrad and K. Borodianskiy, "Bioactive Coating on Ti Alloy with High Osseointegration and Antibacterial Ag Nanoparticles", *ACS Applied Materials & Interfaces*, vol. 11, no. 43, pp. 39534-39544, 2019.

[17] C. Liu et al., "Rapamycin/sodium hyaluronate binding on nano-hydroxyapatite coated titanium surface improves MC3T3-E1 osteogenesis", *PLOS ONE*, vol. 12, no. 2, 2017.

[18] A. Jaafar, C. Hecker, P. Árki and Y. Joseph, "Sol-Gel Derived Hydroxyapatite Coatings for Titanium Implants: A Review", *Bioengineering*, vol. 7, no. 4, p. 127, 2020.

[19] R. Pillai, M. Frasnelli and V. Sglavo, "HA/β-TCP plasma sprayed coatings on Ti substrate for biomedical applications", *Ceramics International*, vol. 44, no. 2, pp. 1328-1333, 2018.

[20] G. Singh, H. Singh and B. Sidhu, "Corrosion behavior of plasma sprayed hydroxyapatite and hydroxyapatite-silicon oxide coatings on AISI 304 for biomedical application", *Applied Surface Science*, vol. 284, pp. 811-818, 2013.

[21] I. Demnati, D. Grossin, C. Combes and C. Rey, *Journal of Medical and Biological Engineering*, vol. 34, no. 1, p. 1, 2014.

CHAPTER 4: REACTIONS AND INTERACTIONS

4.1 Thermodynamics

This section looks at thermodynamics, which is important in order to understand the thermal behaviour of HAp during the coating process. The sections below give an overview of the interactions which occur due to the effect of temperature.

Air plasma spraying was used to deposit the HAp powder on the Ti-6Al-4V substrates. The plasma has been observed to work at extremely high temperatures in the range of 5000-20 000 ℃ and this has the ability to decompose the HAp powder [1]. Thermal decomposition of HAp was reported by Carayon and Lacout [1], when samples of plasma-sprayed HAp were investigated and analysed using XRD. Other researchers also reported on the thermal decomposition of HAp when they injected HAp powder into a plasma, they found that it undergoes thermal decomposition which takes place whilst in the hot plasma jet [2-3]. The behaviour of HAp due to exposure to high temperature depends on the path followed, temperature in the plasma, particle size, structure, composition, dispersibility and synthesis conditions of the HAp samples used [4]. When heating hydroxyapatite, there are 3 stages that are observed i.e.: evaporation of water, dehydroxylation and decomposition [2]. Certain synthesis methods usually contain water which is absorbed into the lattice structure [4]. Therefore, when heated at low temperatures there appears to be evaporation of the water present on the HAp surface and from within the pores leaving behind more ideal HAp. The evaporation does not change the HAp lattice parameters [5]. However, water present in the pores is released as the temperature increases.

4.1.1 HAp Dehydroxylation:

As the temperature increases, dehydroxylation is observed to take place and this is when the hydroxyl (OH) group starts to disappear. This causes the lattice water to be removed therefore causing a contraction in the lattice parameter *a* [4]. Dehydroxylation was reported to take place as the temperature rises to 850-900 ℃ forming vacancies in the HAp structure in the position of the hydroxyl groups [5]. HAp dehydroxylation takes place by firstly transforming into oxyhydroxyapatite (OHA) thereafter forming oxyapatite (OA) with further dehydroxylation [3]. The dehydroxylation of HAp occurs in the following sequence [2-3]:

$$1:\ Ca_{10}(PO_4)_6(OH)_2 \rightarrow Ca_{10}(PO_4)_6(OH)_{2-2x}O_x[\ ]x + xH_2O \qquad (4.1)$$

(hydroxyapatite) → (oxyhydroxyapatite)

$$2:\ Ca_{10}(PO_4)_6(OH)_{2-2x}O_x[\ ]x \rightarrow\ Ca_{10}(PO_4)_6O_x\ [\ ]x + (1-x)H_2O \qquad (4.2)$$

(oxyhydroxyapatite) → (oxyapatite)

The HAp dehydroxylation is dependent on the rate of heating, water vapour partial pressure and kinetic factors [4]. As the temperature increases above 1300 ℃, decomposition of the oxyapatite (OA) starts to take place [5]. The figure 4.1 briefly describes the process. Decomposition forms tricalcium phosphate, tetracalcium phosphate and calcium oxide in the following way [2-3]:

4.1.2 HAp Decomposition:

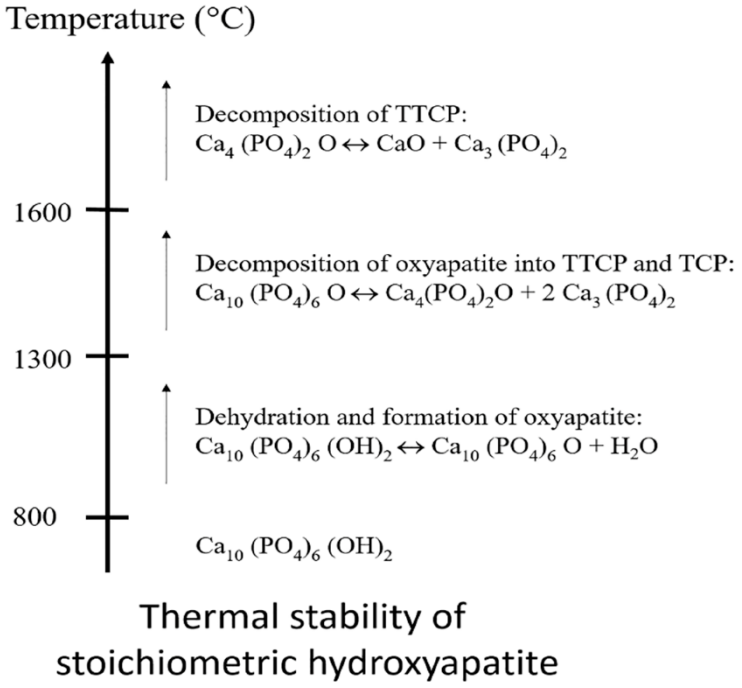

Figure 4.1: *Diagram showing the decomposition of hydroxyapatite. Taken from [6].*

At higher temperatures, oxyapatite decomposes into tricalcium phosphate (TCP) and tetracalcium phosphate (TTCP) with both TCP and TTCP decomposing into CaO by the following reactions:

$$3:\ Ca_{10}(PO_4)_6O_x[\,]x \rightarrow 2Ca_3(PO_4)_2 + Ca_4O(PO_4)_2 \qquad (4.3)$$

(oxyapatite) → (tricalcium phosphate) + (tetracalcium phosphate)

$$4a:\ 2Ca_3(PO_4)_2 \rightarrow 3CaO + P_2O_5 \qquad (4.4)$$

$$4b:\ Ca_4O(PO_4)_2 \rightarrow 4CaO + P_2O_5 \qquad (4.5)$$

where the [ ] represents the vacancies present in the lattice structure of hydroxyapatite in the positions of the OH^- which is along the crystallographic c-axis [2-3]. The decomposition of HAp is affected by the water partial pressure and the rate of heating [4]. As the temperature rises, the material reaches its melting point which occurs at

approximately 1550 ℃ as reported by Levingstone [7]. However, Ma et al. [8] reported the melting point of HAp to be 1500 ℃. Table 4.1 represents the effect on HAp due to change in temperature [7].

Table 4.1: *Table displaying the thermal effects on HAp [7].*

Temperature ℃	**Reactions**
25-600	Absorbed water gets evaporated
600-800	Decarbonation
800-900	Dehydroxylation of HAp
1050-1400	Decomposition of HAp to form β-TCP & TTCP
<1120	β-TCP is stable
1120-1470	β-TCP is converted to –TCP
1550	HAp melting point
1630	TTCP melting point
1730	TCP melting point

4.2 Interactions with SBF

This section focuses on the biochemical interactions taking place between the HAp coating surface and the simulated bodily fluid (SBF). In this study, HAp was coated on Ti-6V-4Al alloy substrate with two different thicknesses. The coated samples were then immersed in SBF for varying number of days (to mimick the biological response of HAp coating within the physiological environment). The sections below give an overview of the interaction which happens to the HAp coating after immersed in the SBF.

4.2.1 Simulated Bodily Fluid

SBFs are used to determine the functioning and biological performance and response of biomaterials [9]. SBFs are salt solutions that contain an ionic concentration similar to that of human blood plasma without enzymes and proteins. There are many different types of SBFs such as ionized simulated fluid (iSBF), conventional simulated fluid (cSBF), modified simulated fluid (mSBF), synthetic simulated fluid (sSBF) and revised simulated fluid (rSBF). These simulated bodily fluids differ due to a difference in ionic species and ionic concentration of species. Kokubo [10] developed a revised simulated bodily fluid (rSBF) which contains an ionic concentration similar to that of human blood plasma but does not include the enzymes and proteins. The rSBF solution is made using distilled water mixed with specific amounts of salts (NaCl, NaHCO3, Na2CO3, KCl, K2HPO4.3H2O, MgCl2.6H2O, CaCl2, Na2SO4). The salts used are also mentioned in table 5.2 (Experimental Procedure). Table 4.2 shows the difference in ionic concentrations of rSBF and human blood plasma.

Table 4.2: *Concentration of ions for blood plasma and rSBF [11].*

Ionic species	Ionic concentration of blood plasma in $\frac{mMol}{l}$	Ionic concentration of *rSBF* in $\frac{mMol}{l}$
Ca^{2+}	2.5	2.5
HPO_4^{2+}	1.0	1.0
Na^{+}	142.0	142.0
Cl^{-}	103.0	103.0
Mg^{2+}	1.5	1.5
K^{+}	5.0	5.0
SO_4^{2-}	0.5	0.5
HCO_3^{-}	27.0	27.0

4.2.2 Incubation in SBF

The substrates coated with HAp powder were immersed in the rSBF for varying periods of time. The ionic concentrations are stated in table 5.3 (Experimental Procedure) and the volume of the SBF used is dependent on the surface area of the coating to be immersed. The temperature of the solution during immersion was kept at an approximate physiological standard of 36 °C. Since the pH of the rSBF had maintained a pH value of 7.25, the pH was kept at a constant by using TRIS (tris-hydroxymethyl-aminomethane) with HCl, HEPES (2-(4-(2-hydoxyethyl)-1-piperazinyl) ethane sulphonic acid) and NaOH as the buffer. During incubation of the coated substrates, biochemical interactions occur between the HAp coating and the SBF. This is known as the *in vitro* response due to HAp being immersed in SBF [10]. There is also a response known as the *in vivo* however this is the response due to studies and experiments taking place within a living organism whereas *in vitro* is the response due to studies and experiments taking place in labware. The *in vitro* response can be classified into two phases i.e.: dissolution of ions from the coating surface thereafter precipitation and these are explained briefly in subsections below:

Dissolution

Dissolution occurs when a solute dissolves in a solvent. In the case of HAp coatings, calcium and phosphorous ions dissolve into the solution due to the presence of a concentration gradient. When dissolving, these ions redistribute so that they can form new bone with the surrounding bone tissue. When the HAp coatings are immersed in the SBF, a dissolution biochemical interaction occurs, changing the chemical composition of HAp. The response depends on the coating technique used [12-14]. These techniques include; electrostatic spray assisted vapor deposition [12], vacuum plasma spraying (VPS), detonation gun spraying (DGUN) [13] and spark plasma sintering (SPS) [14]. The incubation of HAp in the SBF causes the calcium and phosphate ions to rearrange and dissolve in the solution, down the concentration

gradient [12]. The Ca^{2+}, PO_4^{3-} and OH^- from the coating dissolves into the solution which increases the number of electrolytes in the solution up until the solution reaches saturation. The rate of dissolution depends on the ionic concentration of the solution. The concentration gradient disappears when the solution reaches saturation. A solution that is supersaturated would not have further ions dissolving in the solution. The trend appears to be that the concentration of the Ca^{2+} ions increase with immersion time upon reaching a maximum concentration. After reaching a maximum, the concentration starts to decrease due to the formation of a precipitate [15].

Deposition of HAp on the Ti-6Al-4V substrate by air plasma spraying leads to the formation of the thermal products CaO, TCP and TTCP. The phases dissolve in the SBF in the following order with increasing immersion time [16]:

$$HAp < \beta - TCP < \alpha - TCP < TTCP < ACP < DCP < CaO \qquad (4.6)$$

It can be seen from the equation 4.6 above that amorphous calcium phosphate would dissolve at a faster rate as compared to the crystalline calcium phosphate. This behaviour was also reported by Ducheyne et al. [15] and Cao et al. [17]. They indicated that these phases were found to have a higher rate of dissolution than the original HAp due to their low crystallinity and due to being unstable [17]. The are many factors reported to influence the rate of dissolution, these include temperature [18], porosity [19], size of crystals [20] and quantity of impurities present [21]. Majority of the impurities dissolve within the first 10 days of incubation in the SBF. Dissolution leads to a more crystalline coating due to the removal of impurities and amorphous content.

Precipitation

The Ca^{2+} ions have been observed to display a trend in the concentration as stated above i.e., initially the concentration in the solution was found to increase with immersion time up until it reaches maximum concentration where it then starts to decrease [15]. Kokubo et al. [22] reported that after immersion in SBF for a long period, the surface appears to become negatively charged. This causes the Ca^{2+} ions in the solution to be attracted to the surface therefore forming a Ca rich surface [22]. When it reaches a maximum concentration, this is when the solution becomes supersaturated. Precipitation then starts to occur causing a decrease in the concentration of Ca^{2+} ions. Calcium phosphate transforms into the apatite as a result of a chemical reaction taking place at the interface of the surface [22].

The longer the incubation time, the higher the ion concentration of the Ca^{2+} therefore causing the solution to become saturated. This leads to a precipitate forming which consists of apatite crystals [23] that increase in size with immersion time. Precipitation can start to occur within a few hours of immersion to a few weeks after immersion. This precipitate layer acts as a bioconductive layer for the purpose of bone integration.

4.3 References

[1] M. T. Carayon and J. L. Lacout, "Study of the Ca/P atomic ratio of the amorphous phase in plasma-sprayed hydroxyapatite coatings", *Journal of Solid State Chemistry*, vol. 172, no. 2, pp. 339-350, 2003.

[2] M. R. Mansur, "Deposition and Characterization of a Coating from Calcium Phosphate and Titanium Alloy on Austenitic Stainless Steel", PhD, Swinburne University of Technology, 2014.

[3] R. B. Heimann, "Thermal spraying of biomaterials", *Surface and Coatings Technology*, vol. 201, no. 5, pp. 2012-2019, 2006.

[4] N. V. Bulina, S. V. Makarova, S. G. Baev, A. A. Matvienko, K. B. Gerasimov, O. A. Logutenko and V. S. Bystov, "A Study of Thermal Stability of Hydroxyapatite", *Minerals*, vol. 11, no. 12, p. 1310, 2021.

[5] K. Tõnsuaadu, K. A. Gross, L. Plūduma and M. Veiderma, "A review on the thermal stability of calcium apatites", *Journal of Thermal Analysis and Calorimetry*, vol. 110, no. 2, pp. 647-659, 2011.

[6] M. Casas-Luna, M. Horynová, S. Tkachenko and L. Klakurková, "Chemical Stability of Tricalcium Phosphate–Iron Composite during Spark Plasma Sintering", *Journal of Composites Science*, vol. 2, no. 3, p. 51, 2018.

[7] T. Levingstone, "Optimisation of plasma sprayed hydroxyapatite coatings", PhD, Dublin City University, 2008.

[8] J. Ma, X. Ge, N. Pelate and S. Lei, "Numerical investigation of two-dimensional thermally assisted ductile regime milling of nanocrystalline hydroxyapatite bioceramic material", *Ceramics International*, vol. 41, no. 3, pp. 3409-3419, 2015.

[9] A. Oyane, H. Kim, T. Furuya, T. Kokubo, T. Miyazaki and T. Nakamura, "Preparation and assessment of revised simulated body fluids", *Journal of Biomedical Materials Research*, vol. 65, no. 2, pp. 188-195, 2003.

[10] T. Kokubo, S. Ito, Z. T. Huang, S. Sakka, T. Kitsugi, T. Yamamuro, "Ca, P-rich layer formed on high-strength bioactive glass-ceramic A-W", *Journal of Biomedical Materials Research*, vol. 24, no. 3, pp. 331-343, 1990.

[11] A. Oyane, H. Kim, T. Furuya, T. Kokubo, T. Miyazaki and T. Nakamura, "Preparation and assessment of revised simulated body fluids", *Journal of Biomedical Materials Research,* vol. 65, no. 2, pp. 188-195, 2003.

[12] X. Hou, K. Choy and S. E. Leach, "Processing and in vitro behavior of hydroxyapatite coatings prepared by electrostatic spray assisted vapor deposition method", *Journal of Biomedical Materials Research Part A*, vol. 83, no. 3, pp. 683-691, 2007.

[13] H. C. Gledhill, I. G. Turner, C. Doyle, "In vitro dissolution behaviour of two morphologically different thermally sprayed hydroxyapatite coatings", *Biomaterials*, vol. 22, no. 7, pp. 695-700, 2001.

[14] L. G. Yu, K. A. Khor, H. Li and P. Cheang, "Effect of spark plasma sintering on the microstructure and in vitro behavior of plasma sprayed HA coatings", *Biomaterials*, vol. 24, no. 16, pp. 2695-2705, 2003.

[15] S. R. Radin, P. Ducheyne, L. King, "The effect of calcium phosphate ceramic composition and structure on in vitro behavior. II. Precipitation", *Journal of Biomedical Materials Research*, vol. 27, no. 1, pp. 35-45, 1993.

[16] S. R. Radin, P. Ducheyne, L. King, "The effect of calcium phosphate ceramic composition and structure on in vitro behavior. I. Dissolution", *Journal of Biomedical Materials Research*, vol. 27, no. 1, pp. 25-34, 1993.

[17] Y. Cao, J. Weng, J. Chen, J. Feng, Z. Yang, X. Zhang, "Water vapour-treated hydroxyapatite coatings after plasma spraying and their characteristics", *Biomaterials*, vol. 17, no. 4, pp. 419-424, 1996.

[18] C. C. Berndt and K. A. Gross, *Structural Changes of Plasma Sprayed Hydroxyapatite Coatings During In-Vitro Testing*, 5th ed., pp. 589-597, 1997.

[19] J. H. Lin, M. L. Liu and C. P. Ju, "Morphologic variation in plasma-sprayed hydroxyapatite-bioactive glass composite coatings in Hank's solution", *Journal of Biomedical Materials Research*, vol. 28, no. 6, pp. 723-730, 1994.

[20] L. Sun, C. C. Berndt, K. A. Khor, H. N. Cheang and K. A. Gross, "Surface characteristics and dissolution behavior of plasma-sprayed hydroxyapatite coating", *Journal of Biomedical Materials Research*, vol. 62, no. 2, pp. 228-236, 2002.

[21] S. R. Radin and P. Ducheyne, "Plasma spraying induced changes of calcium phosphate ceramic characteristics and the effect on in vitro stability", *Journal of Materials Science: Materials in Medicine*, vol. 3, no. 1, pp. 33-42, 1992.

[22] T. Kokubo, H. Kim and M. Kawashita, "Novel bioactive materials with different mechanical properties", *Biomaterials*, vol. 24, no. 13, pp. 2161-2175, 2003.

[23] M. Topic, T.P. Nstoane and R.B. Heimann, “Microstructural characterization and stress determination in as-plasma sprayed and incubated bioconductive hydroxyapatite coatings”, *Surface and Coatings Technology*, vol. 201, no. 6, pp. 3633-3641, 2006.

CHAPTER 5: EXPERIMENTAL PROCEDURE

5.1 Sample preparation

The medical grade Titanium Aluminium Vanadium (Ti-6Al-4V) substrates were purchased from Biomaterials Limited, North Yorkshire, UK. They were obtained in the form of rods with a diameter of 20 mm. The rods were cut perpendicular to their longitudinal axis into disk and cylinder substrates of thickness 5 mm and 25 mm respectively. Both substrate geometries had a diameter of 20 mm. The substrates were then grit-blasted using alumina particles of the size in the range 0.5 mm to 1 mm so that the coating bonds better to the substrates. This was done at an air pressure of approximately 4 bars. The grit blasting was performed at approximately 90° to the surface of the substrate.

The loose alumina particles were removed from the substrate surface [1] by cleaning the samples in an ultrasonic bath with a 10% Tickopur mixed with deionized water. Substrate immersion was done for approximately 10 minutes at a temperature of 40 °C on a heater plate. The samples were then blow dried with nitrogen. After cleaning, the substrates were mounted on to the sample holder and then deposited with hydroxyapatite using plasma spraying in a number of batches.

Hydroxyapatite was chosen to be deposited on the substrates therefore HAp powder was the feedstock material used for coating the substrates. The powder was obtained from Plasma Biotal Limited, Tideswell, Derbyshire, UK. It was of batch P215, CAPTOL 90. The powder has a size distribution of 120 ± 20 μm. The powder used was of high crystallinity and high purity.

5.2 Plasma-spraying deposition

Plasma spraying is a coating technique whereby the powder to be coated (feedstock) on the substrate is injected into a plasma at very high temperatures of approximately 10000 K [2]. Depending on the type of material, the powder reaches its melting point due to the high temperature in the plasma. Air plasma spraying uses a high energy source to accelerate the powder particles to and over the substrate.

Plasma spraying-deposition was used in this study to deposit the HAp powder on the Ti-6Al-4V substrate. The coating was done in air using a Plasma-Technik M-1000 APS system together with a Sulzer Metco F4 MB plasmatron under atmospheric conditions. The substrates were firmly fixed on a sample support holder as shown in figure 5.1. A screw was used to fasten the top of the sample holder to secure the samples in place. Air plasma spraying was done on the flat surface of the substrates- the grit blasted side.

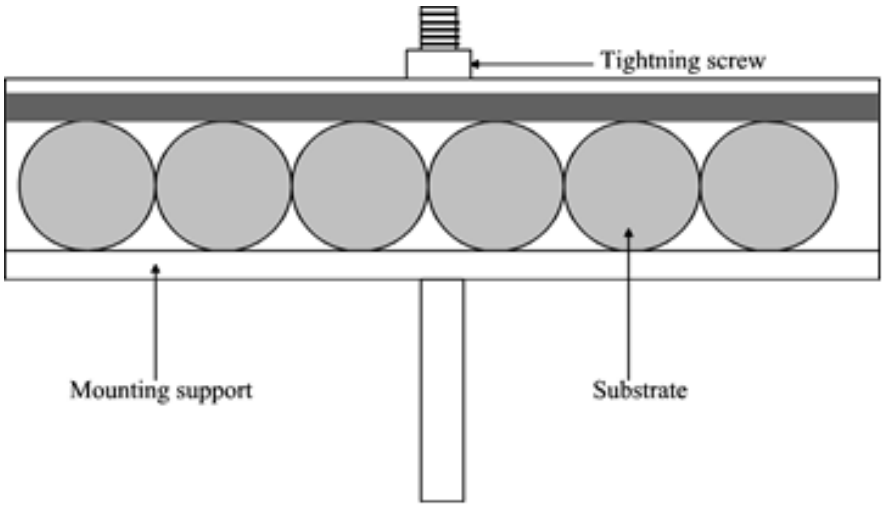

Figure 5.1: *Support used while plasma spraying to firmly mount the Ti-6Al-4V substrates [1].*

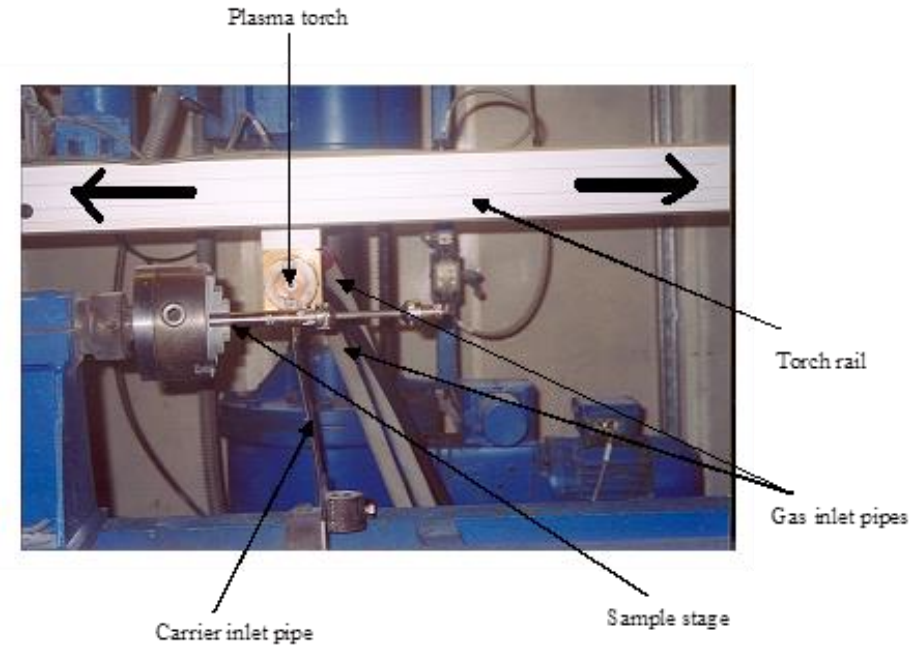

Figure 5.2: *System used for air-plasma spraying the substrates. The torch moves in the direction of black arrows [1].*

The coating process included injecting the feedstock into the plasma at an angle perpendicular to the direction of the plasma plume axis for spraying. Approximately 6 torch passes were completed across the flat substrate surface for coating. Each pass across the surface provided a layer of deposit. While spraying, the torch was held at a distance of 90 mm away from the substrate and at a direction perpendicular to the substrate surface. The torch had a horizontal speed of 0.1 m/s and a transverse speed of 0.017 m/s. The plasma heat was produced by a mixture of argon and hydrogen gas. Argon was also used as the carrier gas to inject the feedstock into the plasma. Coating parameters are shown in table 5.1.

Table 5.1: *Coating parameters used for spraying of Ti-6Al-4V substrates.*

Parameter	Value
Primary plasma gas (Ar)	45 slpm
Secondary plasma gas (H_2)	6.5 slpm
Carrier gas (Ar)	5 slpm
Relative powder feed rate	20 %
Relative hopper stirrer rate	40 %
Spray distance	90 mm
Plasma power	30 kW
Horizontal speed	0.1 m/s
Traverse speed	0.017 m/s

After coating, the samples were then left in the holder to cool down. The coated substrates were then removed from the support and cleaned to get rid of any loose particles using methanol. Figure 5.3 shows a photograph of the substrates after coating the top flat surface of the substrates. The thicknesses of the coatings were determined by measuring the thickness of the substrate before and after spraying with HAp powder using a micrometer and was found to range between 180 and 240 µm.

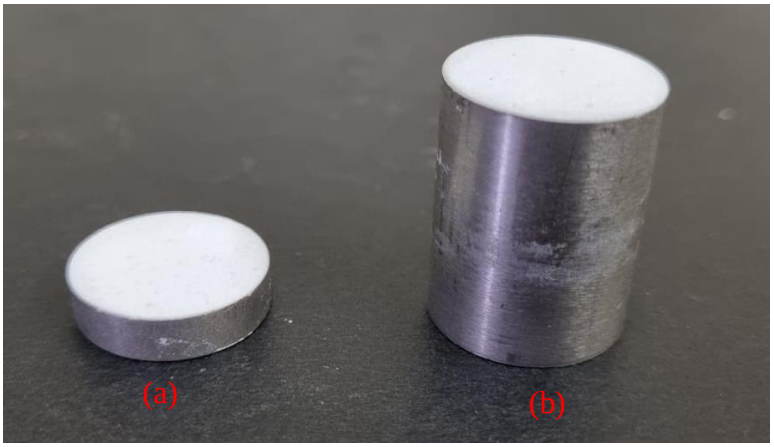

Figure 5.3: *Picture of HAp coated Ti-6Al-4V substrates of different thickness, with the white area at the top surface indicating the coated side: (a) flat disk (b) cylinder.*

5.3 Incubation experiment

After the samples were sprayed with HAp powder, they were immersed in revised simulated bodily fluid (rSBF) for various periods of time (7, 28 & 56 days) in order to study the samples' biological response. Kokubo [3] developed the solution which contains an ionic concentration similar to that of human blood plasma but does not include the enzymes and proteins [3-4]. Incubation in this simulated bodily fluid would allow for the evaluation and observation of the bioactivity of coating *in vitro*. This solution is composed of a various number of salts mixed with deionized water. Table 5.2 gives names of the salts with the proportions used. Table 5.3 displays the ion concentrations of blood plasma, conventional SBF and rSBF.

Table 5.2: *Composition of salts in Kokubo's revised simulated body fluid [4-5].*

Reagent	Concentration [g/l]
NaCl	5.403
$NaHCO_3$	0.736
Na_2CO_3	2.036
KCl	0.225
$K_2HPO_4.3H_2O$	0.238
$MgCl_2.6H_2O$	0.311
HEPES buffer agent	11.928
$CaCl_2$	0.293
Na_2SO_4	0.072

Immersion studies were done by putting the samples in polypropylene boxes and these boxes were then positioned in an incubator. The volume of r-SBF that was needed to incubate a certain area of the substrates is given by:

$$V = \frac{A}{3.33}\, m^{-3} \qquad (5.1)$$

where V is the volume and A is the coated area that is required to be immersed. The temperature and pH of the r-SBF during immersion was kept at a constant of 36 ± 1 ℃ electronically and 7.4, respectively. The pH level was observed electronically and

altered by increasing the proportion of NaOH. The r-SBF was stirred regularly to prevent the formation of precipitates in the solution. Both disk and cylinder samples were immersed in the r-SBF for 7, 28 and 56 days. The samples after immersion were then rinsed using deionized water. The rinsed samples were then dried for 24 hours at a temperature of 100 ℃.

Table 5.3: *Ionic concentration for rSBF compared to human blood plasma [5].*

Ionic species	Ionic concentration of rSBF in $\frac{mMol}{l}$	Ionic concentration of human blood plasma in $\frac{mMol}{l}$	Ionic concentration of *cSBF* in $\frac{mMol}{l}$
Ca^{2+}	2.5	2.5	2.5
HPO_4^{2+}	1.0	1.0	1.0
Na^{+}	142.0	142.0	142.0
Cl^{-}	103.0	103.0	148.8
Mg^{2+}	1.5	1.5	1.5
K^{+}	5.0	5.0	5.0
SO_4^{2-}	0.5	0.5	0.5
HCO_3^{-}	27.0	27.0	4.2

5.4 X-ray Diffraction

X-rays were first discovered on November 8th, 1895, by Wilhelm Conrad Röntgen [6-7]. X-rays are electromagnetic waves which are very much alike to that of visible light but with a very high energy [7]. They contain wavelengths that range from 0.01 nm to approximately 100 nm with energies that range from 100 eV to 100 keV [8]. X-rays lie between gamma-rays and ultraviolet in the electromagnetic spectrum [8]. They are formed when an external beam of energetic electrons interacts with the electrons in the inner shells of the atom [8].

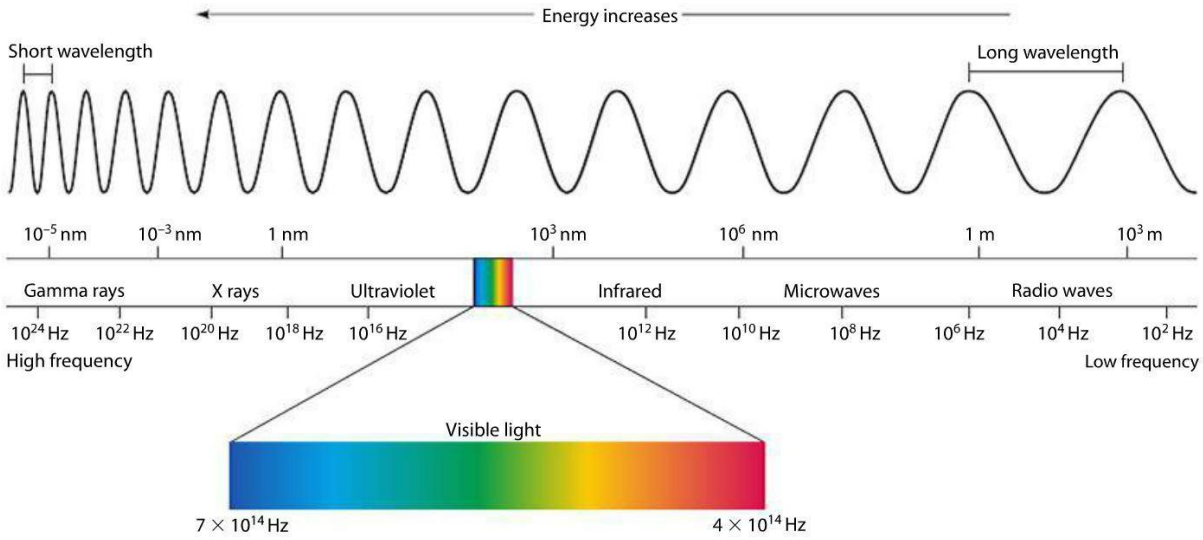

Figure 5.4: *Spectrum of radiation [9].*

X-ray diffraction is a scattering technique that is widely used in different fields of science and engineering for phase identification, crystal structural changes, to measure the texture, the roughness and layer thickness and to identify the residual stress (strain) of the materials [10].

In the XRD setup, a (monochromatic) beam of X-rays is incident on a crystalline material and it gets scattered by different lattice planes. The angle that the incident beam forms with the lattice plane is known as θ while that formed by the scattered beam with respect to the transmitted bean is known as 2θ [11]. The 2θ angle is known as the Bragg angle and it is also known as the angle of maximum intensity. This allows the formulation of Bragg's diffraction condition given by the Bragg equation (5.2) below:

$$n\lambda = 2d \sin\theta \qquad (5.2)$$

where λ is the wavelength of the X-ray, n is the integer with θ being the diffraction angle and d the interatomic spacing.

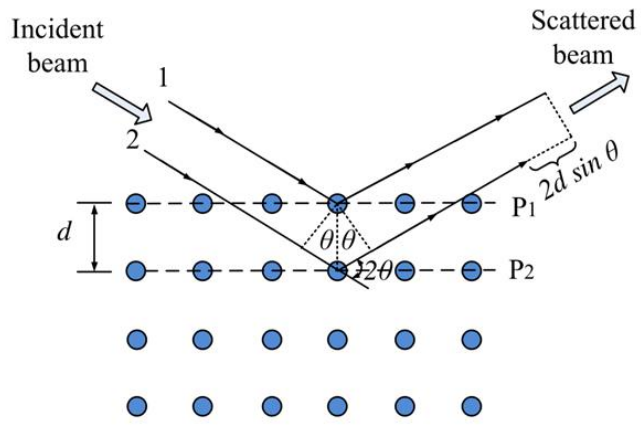

Figure 5.5: *Diagram illustrating Bragg's law for an incident X-ray beam on a crystal lattice plane [12].*

The XRD equipment consists of an X-ray tube, a detector and a sample holder. The X-rays are generated by heating the filament in the cathode, which then produces the electrons. A high voltage accelerates these electrons, which in turn strike the target material. Characteristic X-rays are generated when the electrons produced have adequate energy to remove the inner shell electrons of the sample. The X-rays generated are focused and collimated on the target sample. The sample rotates with the collimated X-ray beam, and this occurs at angle θ while the X-ray detector, which gathers the

diffracted rays, occurs at an angle 2θ. The detector and sample are on one side. The goniometer is the instrument that controls the angle the sample is at. The intensities of the scattered X-rays are monitored and listed whilst the sample and detector rotate on the same side. When the incident X-rays target the sample and satisfies Bragg's equation, constructive interference occurs, and a peak is observed [13]. A detector collects the peak information and transforms the signal to a count rate which is then recorded by the computer monitor.

The X-ray beam consists of several components, the most generally known are K_α and K_β. K_α is made up of $K_{\alpha1}$ and $K_{\alpha2}$, where the $K_{\alpha1}$ has twice the intensity and a lower wavelength than that of $K_{\alpha2}$. The target material determines the specified wavelength. The wavelength of $K_{\alpha1}$ and $K_{\alpha2}$ are almost alike and thus the weighted average between the two wavelengths is determined and used. In this study, copper is the target material with Cu K_α radiation.

5.4.1 Phase Identification

The X-ray diffraction experiments were conducted using the setup at the South African Nuclear Energy Corporation (NECSA). A Bruker D8 Advanced diffractometer was used for the phase analysis and identification, see figure 5.6. The diffractometer uses Cu radiation, and the data is collected with a Lynx eye position sensitive detector (PSD). Instrument optics include a goebel mirror and 2.5° soeller slits on the primary side and Lynx Iris and 2.5° soeller on the secondary side. A locked couple scan was used for the measurements. Measurements were carried out with step size of 0.02° at 2 s per step in the 2θ range 15° to 100°. Qualitative and quantitative analysis were done using ICDD PDF-4+ database with Sieve software and TOPAS v4.2 (TOPAS-ACADEMIC v4.2, Coelho Software, Brisbane, Australia, 2007) respectively. The software can also be used for the evaluation of the crystallinity of the sample surface.

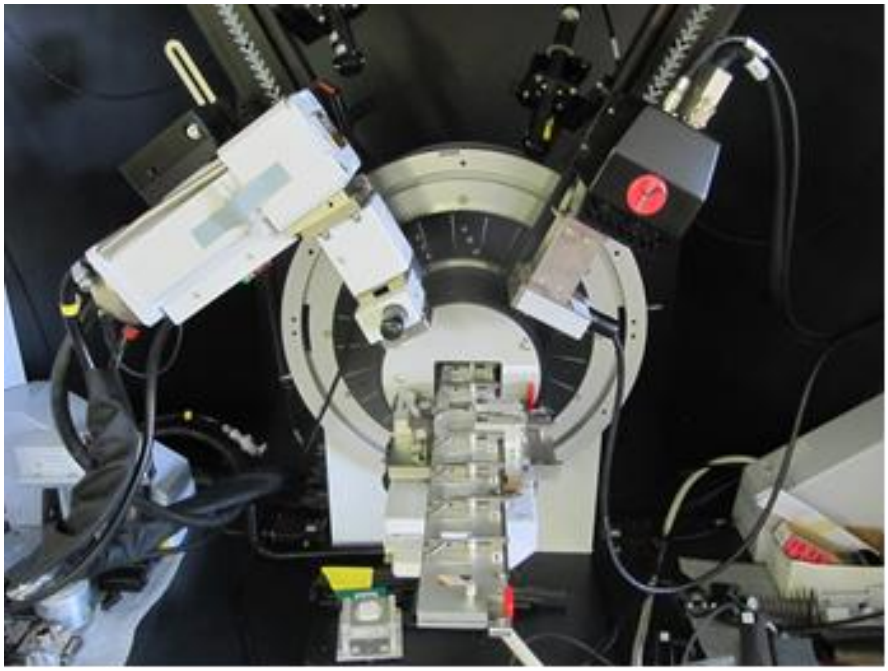

***Figure 5.6**: Picture of the Bruker D8 Advanced diffractometer.*

5.4.2 Residual Stress

5.4.2.1 Definition

Stress and strain are the two quantities that define the nature of the externally applied force on a body and the resulting deformation on that body. Stress is a symmetric tensor of fourth rank and of 9 components, therefore only 6 components are independent. Stress is a tensor given by:

$$\sigma_{ij} = \begin{pmatrix} \sigma_{11} & \sigma_{12} & \sigma_{13} \\ \sigma_{21} & \sigma_{22} & \sigma_{23} \\ \sigma_{31} & \sigma_{32} & \sigma_{33} \end{pmatrix} \qquad (5.3)$$

with the *i-index* representing the direction of traction and the *j*-index representing the normal of the plane on which the traction acts. The off-diagonal components indicate what the shear stress is while the diagonal components indicate the normal stress.

The strain is measured by the diffractometer. The strain is a tensor like stress mentioned above, given by:

$$\varepsilon_{ij} = \begin{pmatrix} \varepsilon_{11} & \varepsilon_{12} & \varepsilon_{13} \\ \varepsilon_{21} & \varepsilon_{22} & \varepsilon_{23} \\ \varepsilon_{31} & \varepsilon_{32} & \varepsilon_{33} \end{pmatrix} \qquad (5.4)$$

It is also a symmetric tensor therefore having 6 independent components. Stress and strain are completely different physical quantities however Hooke's law relates the two quantities by the following formulae:

$$\sigma_{ij} = C_{ijkl}\varepsilon_{kl} \qquad (5.5)$$

and

$$\varepsilon_{ij} = S_{ijkl}\sigma_{kl} \qquad (5.6)$$

with C_{ijkl} the components of elastic stiffness and S_{ijkl} the components of elastic compliance tensor and where the properties of the material determine the elastic constants in the material.

Depending on the sign, stress can be compressive or tensile. When the force applied on a body, results in the stretch of the material, it is known as tensile stress [14]. Compressive stress is the force that results in the deformation of the material such that the material volume reduces [14]. The total stress would be the stress experienced by a part/component or implant in this case while in operation. The total stress on the implant is the sum of the applied stress and the residual stress.

Residual stresses are the stresses that are generated during manufacturing or processing of the desired component of interest [15]. Since they exist in the absence of external forces, they are also referred to as locked in stresses [15]. They are can also be defined as the stress that exists in a material that is at equilibrium or a stationary body [15].

Based on their length scale, they can be classified into 3 categories namely, macroscopic stresses (type 1), microscopic stresses (type 2) and submicroscopic stresses (type 3) [16]. Macroscopic residual stresses are produced during the manufacturing process on a scale that is large relative to the grain size of the material. Microscopic residual stresses on the other hand are generated during the manufacturing process and covers a scale relative to the grain size. Submicroscopic residual stresses are produced due to crystalline defects within the grain [16].

5.4.2.2 Sources of residual stresses

Residual stresses can arise from numerous sources such as a difference in thermal expansion coefficient between two materials, non-uniform plastic deformation within a component, phase transformation and the existence of thermal gradients [15][17]. Examples include; surface preparation and modification such as coating, shot peening and polishing as well as in welds. The residual stresses of a component can be classified according to how it was generated i.e.: thermal, chemical, and mechanical [15]. Manufacturing processes that result in non-uniform plastic deformation is what is known as mechanically generated residual stresses. These stresses can either be produced naturally during the process or be generated in the material purposely with the intention of attaining a specific stress profile for performance enhancement. Processes producing stresses that are undesirable on the material are welding, machining, grinding and rod drawing. These processes produce tensile residual stresses whereas stresses introduced in a material for beneficial purposes are usually compressive in nature. The former promotes crack growth and propagation that can lead to catastrophic component failure while the latter helps to prevent brittle fracture and arrests crack growth [18]. Compressive residual stresses can be obtained by toughening of glass, cold expansion of holes and shot peening amongst others. Thermally generated residual stresses are a result of cooling operations and non-uniform heating [19]. The main cause of thermally generated stresses is the difference in the coefficient of thermal expansion (CTE) leading to different cooling rates. This could eventually lead to a

thermal gradient present since there is also constraints of the material present. Volume changes relating to chemical reactions, phase transformation and precipitation result in chemically generated stresses [15][19].

5.4.2.3 Residual stresses in plasma sprayed coatings

Coating substrates is an application used to combine desirable properties of different materials. Although, there are many coating techniques available as mentioned in Chapter 1 and 3, plasma spraying is used in this investigation. Although coating substrates have led to exceptional results it has also allowed the introduction of some undesired results. During substrate coating, residual stresses are produced which, if too large, could compromise the long-term stability of the coated sample. Large residual stresses often lead to plastic deformation which can result in distortion of the body [19]. The following coating techniques have been found to have residual stress generated upon sample preparation: air plasma spraying [20], sputter deposition [21], chemical vapor deposition [22], laser ablation deposition [23], electron beam physical vapor deposition [24].

The total residual stress generated by air plasma spraying is a combination of thermal, intrinsic stresses sometimes referred to as quenching stresses and phase transformation stresses. Thermal stresses arise from the mismatch of the coefficient of thermal expansion (CTE) between the substrate and the coating. This happens when the coating-substrate system, which after spraying is at an elevated temperature, cools down to room temperature. Depending on the CTE of the coating and substrate materials and their relative thickness, thermal stresses can be tensile or compressive. The intrinsic stresses on the other hand are generated due to the quenching effect of the substrate on the impinging molten droplet. The quenching stress appears due to the molten droplets cooling rapidly when it comes into contact with the relatively cold substrate. The droplets, upon contact, quenches, solidifies, and cools down to the temperature of the substrate and the dimensions of the particle contract according to the temperature it

decreases to [25]. The contraction of the dimensions depends on how well the particles are attached to the substrate surface [25]. As it becomes constrained by the substrate, tensile stress starts to build up within the splat. The magnitude of quenching stress is proportional to the difference in temperature as shown by following formula [25]:

$$\sigma_q = E_c \times \alpha_c (T_c - T_{sub}) \qquad (5.7)$$

with E_c being the Youngs Modulus, α_c is the coefficient of thermal expansion (CTE) of the splat, T_c is the temperature of the droplet on impact and T_{sub} the temperature of the substrate. Quenching stresses are therefore always tensile.

Phase transformation stresses as the name suggests are stresses generated as a result of changes in crystallographic phases. The associated lattice mismatch resulting from the different phases lead to the generation of stress and depending on the sign the stresses can be compressive or tensile.

5.4.2.4 Techniques for residual stresses determination

Modern technology allows accurate determination of stresses that exists within a material using different techniques. There are a number of techniques currently used to measure strain and from this, the residual stresses can be determined. They are grouped in the following categories: destructive and nondestructive. These include hole drilling [26], magnetic methods [27], curvature test [28], thermoelastic methods [29], photo elastic methods [30] and diffraction methods [31]. In this study diffraction methods, due to its non-destructive nature, will be employed. Depending on the type of probe/radiation used, diffraction techniques can either be: neutron diffraction [32], electron diffraction [33] and X-ray and synchrotron diffraction. In this study, laboratory X-rays due to the high flux, shallow penetration (comparable to coating thickness) and being readily available as opposed to neutrons will be used. Neutron diffraction due to low flux has long measurement times as opposed to synchrotron and X-ray radiation.

Neutrons penetrate deeper therefore the diffraction pattern would include peaks from the underlying titanium substrate. Laboratory X-ray diffraction technique is used in this investigation due to the non-destructive and versatile nature. Laboratory X-ray diffraction is also readily available in the labs as opposed to radiation at a large-scale facility such as a synchrotron and nuclear reactor.

When a crystalline body is under tension, the crystallographic lattice spacing decreases and when the body is under compression, the lattice spacing increases. For a 1-dimensional diffraction pattern, this change in lattice spacing is reflected by the change in position of the peak through Bragg's equation (5.2). For a 2-dimensional diffraction pattern, this change is reflected by distortion from a perfect circle to an oval. The sample to be investigated is mounted in the diffractometer and irradiated with the X-ray beam at the point of interest on the surface thereby generating a diffraction pattern, the diffraction peak to be used for stress determination is identified. The position of the peak of interest is measured for different combinations of azimuth, ϕ, and tilt, ψ, angles. The lattice spacing, d, is then determined from the peak position using Bragg's equation (5.2). Using the stress-free lattice spacing, d_0, the corresponding strain is calculated. The calculated strain is converted to stress using Hooke's law, equation (5.5) and (5.6). Figure 5.7 illustrates the relation between the azimuth, tilt angle and sample, Si, and laboratory, L_i, reference frames.

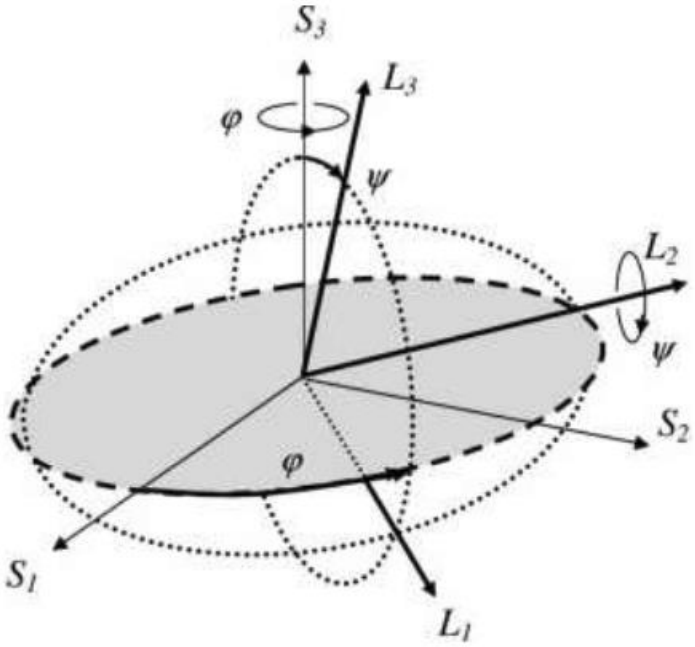

Figure 5.7: *Schematic diagram illustrating the relation of the relative orientation of the laboratory and sample reference frames [34].*

Residual stress in the near-surface region was investigated using a Bruker's D8 Discover instrument shown in figure 5.8. The instrument consists of a ¼ Eulerian cradle and a vertical theta-2theta goniometer. As with the Advance instrument, the diffractometer is equipped with Cu tube however operates in point focus. Primary side optics consisted of a graphite monochromator and 0.8 mm collimator. No optics were mounted on the secondary side. Based on peak intensity and little overlap with other peaks, the (213) HAp reflections corresponding to ~49° 2θ were selected for the investigation. Measurements were done at 6 azimuth orientations, ϕ and ϕ+180° with ϕ =0°, 45° and 90°. For each azimuth angle, a set of 6 tilt angles ψ in steps of 10° was measured. The diffracted data is collected with an area detector, Vantec500. Analysis of the data for residual stress was done using the Leptos v6.02 software [35].

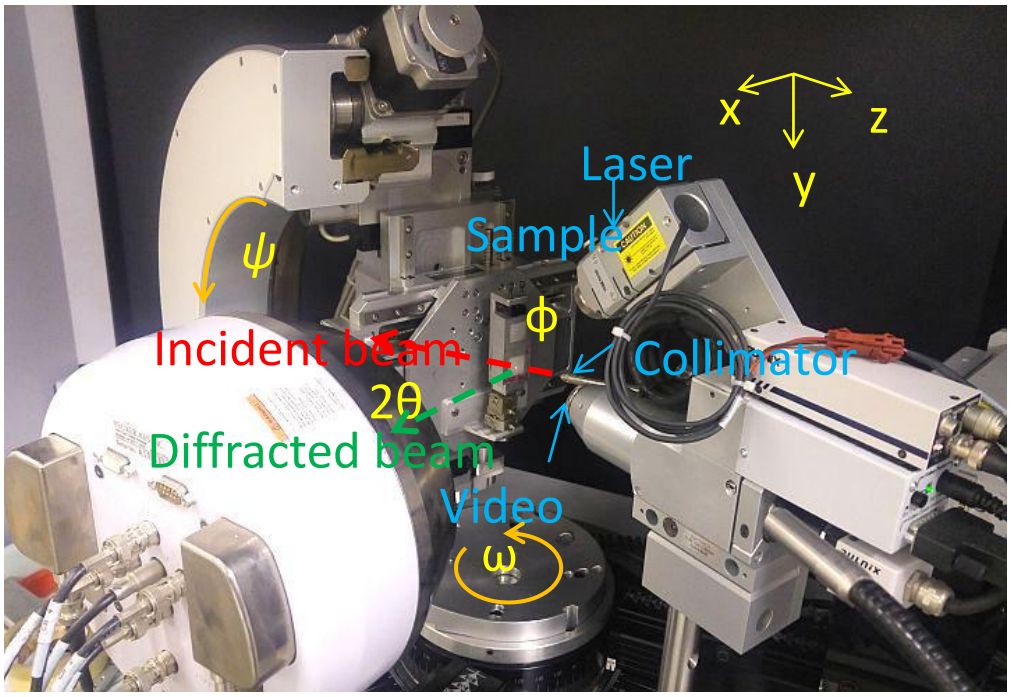

***Figure 5.8**: Picture of the D8 Discover diffractometer for stress strain investigation [1].*

For better statistics, measurements were done mostly on 2 samples from each batch. Due to time constraints only one sample for the 56 days immersed flat disk could be measured hence less data points. The residual stress for each sample was measured at 5 points on the surface to determine if the stress was homogenous across the surface. Figure 5.9 shows the points measured on each sample.

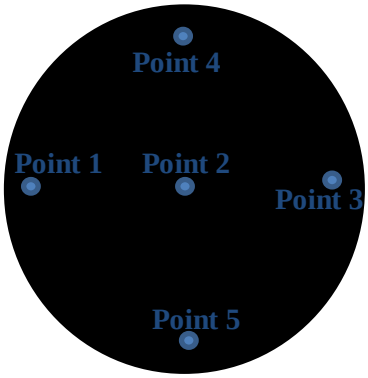

***Figure 5.9:** Figure displaying the 5 points measured on each sample.*

5.5 Scanning Electron Microscopy (SEM)

The scanning electron microscope (SEM) was invented in 1938 by Von Ardenne and is used to study metals, ceramics materials, semiconductor materials, medical science materials and biology specimens [36]. It is a microscope that makes use of electrons to produce a high-resolution image of the surface of samples and is used to study the surface morphology, topography, chemical composition, and crystal structure of a sample [36-37]. The use of electrons in microscopes were developed since light microscopes contain certain drawbacks [36]. The main drawback being low resolving power therefore limiting its resolution [36] [38-39]. Light microscopes have a low magnification and a poor-quality view of the sample surface [39]. SEM is the most well-known versatile instrument that allows one to obtain a high-resolution, accurate and precise image of the sample [36]. This visual image is of great quality with a spatial resolution of 1 nm [36].

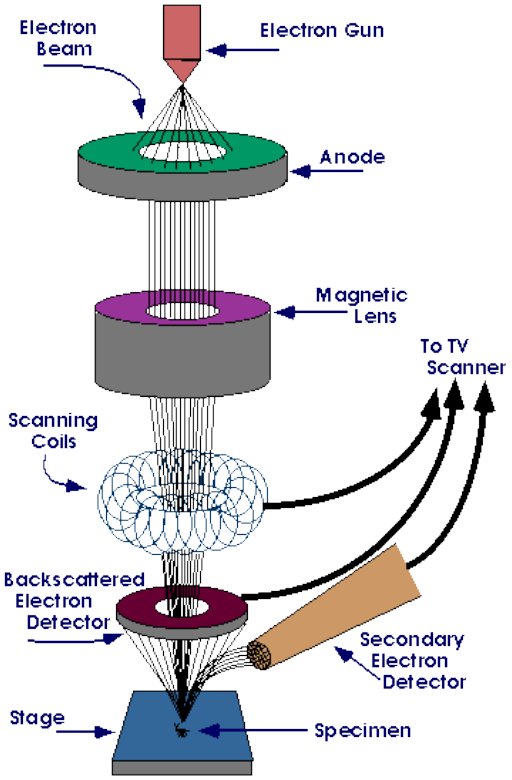

Figure 5.10: *Diagram illustrating process taking place when using SEM, taken from [40].*

The scanning electron microscope generates an image using a beam of electrons which is produced by an electron gun [41]. There exist three types of electron guns, namely: field emission, tungsten hairpin and tantalum hexaboride (LaB6) [42]. A field emission gun (FEG) was used in this study. The FEG has a wire with a sharp metal (usually tungsten) tip with a radius of 100 nm or less [42]. Electrons are emitted when the magnitude of the electric field of the sharp metal amounts to approximately 10 V/m [43]. These emitted electrons are mainly accelerated in the direction of the anode with a bias which is adaptable from 200 V to 300 kV. There are two different types of field electron guns, namely: Schottky field and cold emission gun. Both types require ultra-high vacuum conditions to guarantee that the cathode surface is clean and clear of any contaminants. The tip is cleaned by heating it for a few seconds at approximately 2500K before operating the machine [37]. The electrons that are accelerated form a beam by electromagnetic field lenses to focus on the sample. A scan generator caused by a pair of deflector coils rasters the beam across the surface of the sample [42].

When electrons strike the sample, these incident electrons cause electrons to be scattered within the near-surface region of the material via elastic and inelastic scattering. Figure 5.11 shows the interactions taking place between the electron beam and the sample. This gives rise to particles being released from the sample. These particles contain information from the sample which is provided to the detectors. The information particles are backscattered electrons, characteristic X-rays, secondary electrons and transmitted electrons [44].

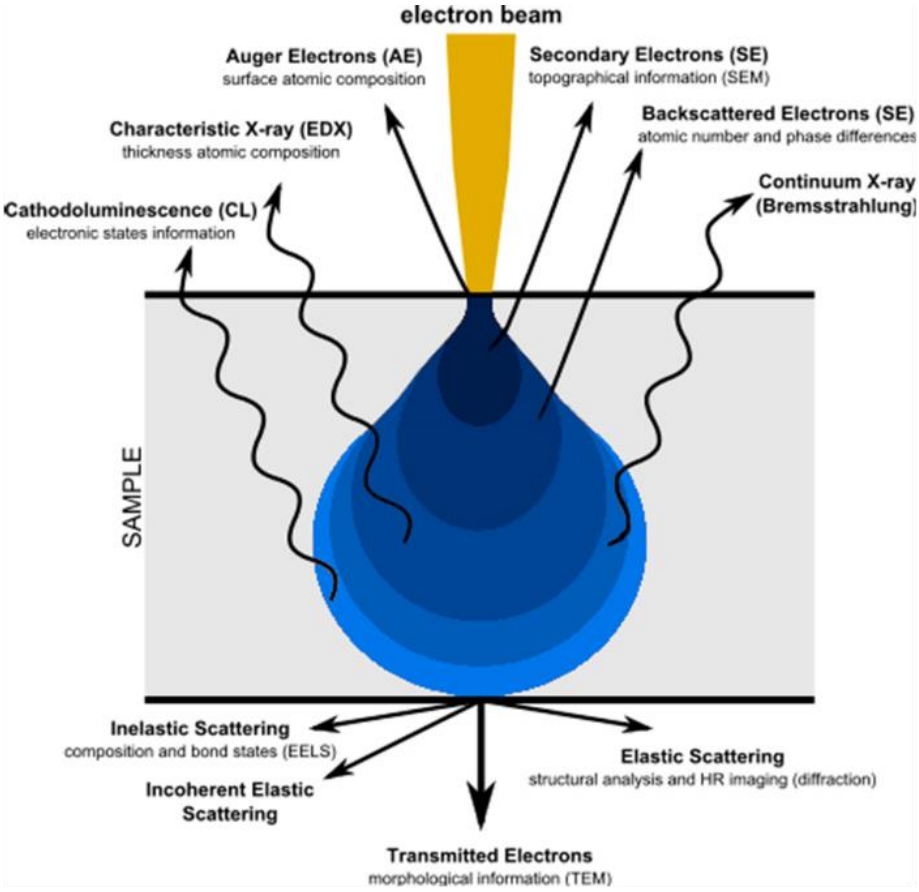

Figure 5.11: *Diagram illustrating the interactions taking place between the electron beam and sample with the particles formed [45].*

The incident electrons collide with the electrons of the sample in inelastic collisions. The target sample as a result produces secondary electrons. Secondary electrons (SE) used in a SEM have energies which are less than 50 eV [46]. The secondary electrons which escape from the sample generate topographical images [43]. Secondary electrons are very close to the surface (< 10 nm) and most of them are absorbed by the sample since they have very low energies [37][47]. Only secondary electrons within the detector's collection range can be detected. A contrast in the image is caused by a variation in the electron intensity. The place where the secondary electron is released determines the contrast of the surface [44]. The edge usually appears brighter since electrons can easily break away at the edge.

The electrons which result due to elastic collisions between the incident beam and the nucleus of the target sample are known as backscattered electrons (BSE). Backscattered electrons give information from the more inner region of the sample since they contain a higher energy than secondary electrons. These electrons generate information for the topography and composition of the target sample. Areas with different chemical compositions will have a different contrast [37]. Such that the area containing an element with a high atomic number appears bright as compared to areas containing elements with lower atomic numbers [47]. Insulators usually absorb the incident electrons thus causing the surface of the sample to be charged up distorting the image and making it appear bright. This however provides inaccurate information about the target sample. Therefore, insulators are coated with a conductive film.

The Zeiss Crossbeam 540 FEG SEM from the University of Pretoria was used in this investigation to analyse the sample surface morphology and the elemental composition on the sample surface. This microscope has a secondary in-lens detector with SE and BSE. The in-lens was used, and it is able to observe SE from the surface that comes from the incident beam. Energy filtering is used together with in-lens detection to form the SEM image. The surface analysis of both sample geometries was done with a beam energy of 1.00 kV.

5.6 Energy Dispersive X-ray Spectroscopy

Energy dispersive x-ray spectroscopy (EDS or EDX) is an analytical technique usually operated together with scanning electron microscopes (SEM) or transmission electron microscopes (TEM) [48]. EDS is used for quantitative elemental and compositional analysis of materials. Therefore, the elemental composition of a material can be obtained using EDS [48]. The composition of the material can be obtained as a point layout and as a map for the different elements [49]. The electron microscope produces a beam of electrons which is aimed at the sample [49-50]. These primary incident electrons strike the sample atoms, and this causes the electrons of the sample to be

released from the inner shells therefore generating electron vacancies [49-50]. The atom becomes unstable due to the electron vacancies present therefore the outer energy level electrons fill the inner shell vacancies [48]. X-rays are produced when this occurs [48]. Since the higher energy level electrons contain a higher amount of energy as compared to those in the inner shell, the energy difference between the two is therefore emitted in the form of X-ray photons. These X-rays photons contain an energy which is unique and characteristic to the element they were emitted from. Thus, every element in a sample contains and produces its own unique X-ray emission pattern [48-49].

These emitted X-rays from the sample are collected by a detector in EDS for analysis of the composition of the sample [51]. The characteristic X-rays of the various elements in the sample gets filtered by the detector into a spectrum and by analyzing this spectrum, the elemental composition of the sample can be obtained [49].

When the incident X-ray is emitted, the detector collects this and transforms the energy of each X-ray to a voltage signal that is proportional to the energy of the X-ray [49]. The process occurs in 3 steps, i.e.:

- *Step 1:* The semiconductor crystals ionize the atoms, and this changes the X-rays to charge pulses.
- *Step 2:* A charge-sensitive preamplifier changes each individual charge pulse to a voltage signal.
- *Step 3:* This voltage signal is sent for processing to the multichannel analyser.

The multichannel analyser modifies the voltage and gives it out as a ‘ramp’. The ramp contains voltage steps where each step correlates to its distinct X-ray energy. Each incident X-ray contains its own energy, and this is transmitted to the computer to present on the screen for analysis and evaluation purposes [49].

The Zeiss Crossbeam 540 FEG SEM with EDS from the University of Pretoria was used in this investigation to analyse the elemental composition of the two different geometry substrates, coated with HAp, before and after immersion in the SBF. Various amounts of measurements were taken from 3 different regions on the surface of every sample.

5.7 References

[1] T. P. Ntsoane, “In-vitro investigation of air-plasma sprayed hydroxyapatite coatings deposited on two geometrically different substrates”, PhD, University of Pretoria, 2020.

[2] H. Xu and H. Guo, Thermal barrier coatings. Philadelphia, *PA: Woodhead Pub*., 2011.

[3] T. Kokubo, S. Ito, Z. T. Huang, T. Hayashi, S. Sakka, T. Kitsugi and T. Yamamuro, “Ca, P-rich layer formed on high-strength bioactive glass-ceramic A-W”, *Journal of Biomedical Materials Research*, vol. 24, no. 3, pp. 331-343, 1990.

[4] H. M. Kim, T. Miyazaki, T. Kokubo and T. Nakamura, “Revised Simulated Body Fluid”, *Key Engineering Materials*, vol. 192-195, pp. 47-50, 2001.

[5] A. Oyane, H. M. Kim, T. Furuya, T. Kokubo, T. Miyazaki and T. Nakamura, “Preparation and assessment of revised simulated body fluids”, *Journal of Biomedical Materials Research*, vol. 65, no. 2, pp. 188-195, 2003.

[6] R. F. Mould, “Röntgen and the discovery of X-rays”, *The British Journal of Radiology*, vol. 68, no. 815, pp. 1145-1176, 1995.

[7] “X-rays”, *Nibib.nih.gov*, 2022. [Online]. Available: https://www.nibib.nih.gov/science-education/science-topics/x-rays. [Accessed: 6- Apr- 2022].

[8] C. Suryanarayana and M. Grant Norton, *X-Ray Diffraction: A Practical Approach*. New York: Springer Science+Business Media, pp. 3-19, 1998.

[9] M. Physics, “The Electromagnetic Spectrum”, *Mini Physics*, 2022. [Online]. Available: https://www.miniphysics.com/electromagnetic-spectrum_25.html#:~:text=The%20main%20components%20of%20the,shortest%20wavelengths%20and%20highest%20frequencies. [Accessed: 18- May- 2022].

[10] J. I. Langford and D. Louer, “Powder diffraction”, vol. 59, no. 2, 1996.

[11] R. Nave, “Bragg’s Law”, *Hyperphysics.phy-astr.gsu.edu*, 2021. [Online]. Available: http://hyperphysics.phy-astr.gsu.edu/hbase/quantum/bragg.html. [Accessed: 20- Aug- 2021].

[12] E. G. Njoroge, “Solid-state interactions between Zr thin films and SiC”, PhD, University of Pretoria, 2014.

[13] D. J. Henry, N. Eby, J. W. Goodge and D. Mogk, “X-ray reflection in accordance with Bragg’s Law”, *Geochemical Instrumentation and Analysis*, 2021.

[14] L. Mshumi, “What Is Stress and Strain? Stress-Strain Curve, SI Units,” *BYJUS*, 2020. [Online]. Available: https://byjus.com/physics/stress-and-strain/. [Accessed: 05- October- 2022]

[15] O. Anderoglu, “Residual Stress Measurement Using X-ray Diffraction,” MSc, Texas A&M University, 2004.

[16] A. Tabatabaeian, A. R. Ghasemi, M. M. Shokrieh, B. Marzbanrad, M. Baraheni, and M. Fotouhi, “Residual Stress in Engineering Materials: A Review,” *Advanced Engineering Materials*, vol. 24, no. 3, pp. 2100786, 2021.

[17] “Residual Stress,” *Industrial Metallurgists*, 2016. [Online]. Available: https://www.imetllc.com/residual-stress/. [Accessed: 05- October- 2022]

[18] “Residual stress” *Wikipedia*, 2022. [Online]. Available: https://en.wikipedia.org/wiki/Residual_stress#:~:text=A%20material%20having%20compressive%20residual. [Accessed: 05- October- 2022]

[19] “What is Residual Stress?” *TWI Global*. [Online]. Available: https://www.twi-global.com/technical-knowledge/faqs/residual-stress#:~:text=Residual%20stresses%20are%20those%20stresses.[Accessed: 05- October- 2022]

[20] B. P. Croom, C. Bumgardner, and X. Li, “Unveiling residual stresses in air plasma spray coatings by digital image correlation,” *Extreme Mechanics Letters*, vol. 7, pp. 126–135, 2016.

[21] J. Hubertus, S. Croce, J. Neu, G. Rizzello, S. Seelecke, and G. Schultes, “Influence of Residual Stresses of Sputtered Thin Film Electrodes for Dielectric Elastomer Applications,” *The 1st International Electronic Conference on Actuator Technology: Materials, Devices and Applications*, 2020.

[22] S. Eroglu and B. Gallois, “Residual stresses in chemically vapor deposited coatings in the Ti-C-N system,” *Le Journal de Physique IV*, vol. 03, no. C3, pp. C3-155C3-162, 1993.

[23] D. V. N. Harish, A. Bharatish, H. N. N. Murthy, B. Anand, and K. N. Subramanya, “Investigation of thermal residual stresses during laser ablation of tantalum carbide coated graphite substrates using micro-Raman spectroscopy and COMSOL multiphysics,” *Ceramics International*, vol. 47, no. 3, pp. 3498–3513, 2021.

[24] J. Cheng, E. H. Jordan, B. Barber, and M. Gell, “Thermal/residual stress in an electron beam physical vapor deposited thermal barrier coating system,” *Acta Materialia*, vol. 46, no. 16, pp. 5839–5850, 1998.

[25] S. Kuroda and T. W. Clyne, “The quenching stress in thermally sprayed coatings,” *Thin Solid Films*, vol. 200, no. 1, pp. 49–66, 1991.

[26] “Hole drilling method – Residual stress measurements by the hole-drilling method – Sint Technology,” *Sintech*. [Online]. Available: https://sint-technology.com/hole-drilling-method/. [Accessed: 05- October- 2022].

[27] S. Abuku and B. D. Cullity, “A magnetic method for the determination of residual stress,” *Experimental Mechanics*, vol. 11, no. 5, pp. 217–223, 1971.

[28] J. Wang, P. Shrotriya, and K.-S. Kim, “Surface Residual Stress Measurement Using Curvature Interferometry,” *Experimental Mechanics*, vol. 46, no. 1, pp. 39–46, 2006.

[29] R. J. Greene, E. A. Patterson, and R. E. Rowlands, “Thermoelastic Stress Analysis,” *Springer Handbook of Experimental Solid Mechanics*, pp. 743–768, 2008.

[30] E. J. Hearn, “Experimental Stress Analysis,” *Mechanics of Materials 2*, pp. 166–192, 1997.

[31] J. Repper, M. Hofmann, C. Krempaszky, B. Regener, E. Berhuber, W. Petry, E. Werner, “Effect of macroscopic relaxation on residual stress analysis by diffraction methods,” *Journal of Applied Physics*, vol. 112, no. 6, p. 064906, 2012.

[32] “Stresstech Bulletin 12: Measurement Methods of Residual Stresses,” *Stresstech*, 2018. [Online]. Available: https://www.stresstech.com/stresstech-bulletin-12-measurement-methods-of-residual-stresses/. [Accessed: 05- October- 2022].

[33] A. M. Korsunsky, *A Teaching Essay on Residual Stresses and Eigenstrains*. Butterworth-Heinemann, 2017.

[34] U. Welzel, J. Ligot, P. Lamparter, A. C. Vermeulen, and E. J. Mittemeijer, “Stress analysis of polycrystalline thin films and surface regions by X-ray diffraction,” *Journal of Applied Crystallography*, vol. 38, no. 1, pp. 1–29, 2005.

[35] Diffrac. Suite Software. [Online]. Available: https://www.bruker.com/en/products-and-solutions/diffractometers-and-scattering-systems/x-ray-diffractometers/diffrac-suite-software.html

[36] S. K. Sharma, D. S. Verma, L. U. Khan, S. Kumar and S. B. Khan, *Handbook of Materials Characterization*. Cham: Springer, 2018.

[37] T. T. Hlatshwayo, “Diffusion of silver in 6H-SiC”, PhD, University of Pretoria, 2010.

[38] P. J. Evennett and C. Hammond, “MICROSCOPY | Overview”, *Encyclopedia of Analytical Science*, pp. 32-41, 2005.

[39] Y. Smith, “Limitations of Optical Microscopy”, *News-Medical*, 2018.

[40] “Scanning Electron Microscope – Radiological and Environmental Management – Purdue University”, *Purdue.edu*, 2021. [Online]. Available: https://www.purdue.edu/ehps/rem/laboratory/equipment%20safety/Research%20Equipment/sem.html. [Accessed: 14- Aug- 2021].

[41] W. Zhou and Z. L. Wang, *Scanning Microscopy for Nanotechnology – Techniques and Applications*. New York: Springer, 2010.

[42] B. Hafner, *Scanning Electron Microscopy Primer*. Twin Cities, pp. 1-29, 2007.

[43] O. S. Odutemowo, “Modification of glassy carbon under strontium ion implantation”, MSc, University of Pretoria, 2021.

[44] T. T. Thabethe, “The interfacial reaction and analysis of W thin film on 6H-SiC annealed in vacuum, hydrogen and argon”, PhD, University of Pretoria, 2017.

[45] “Scanning electron microscopy (SEM), what is it for?”, *ATRIA Innovation*, 2021. [Online]. Available: https://www.atriainnovation.com/en/scanning-electron-microscopy-uses/. [Accessed: 14- Aug- 2021].

[46] E. Velasco, “Scanning Electron Microscopy (SEM) images as a mean to determine dispersibility”, MSc, Iowa State University, 2013.

[47] B. Voutou and E. C. Stefanaki, Electron Microscopy: The Basics. *Thessaloniki: Physics of Advanced Materials Winter School*, 2008.

[48] I. Yadroitsev, I. Yadroitsava, A. Du Plessis and E. MacDonald, *Fundamentals of laser powder bed fusion of metals*, 1st ed. Elsevier, 2021.

[49] S. Biira, "Construction of a chemical vapour deposition reactor and the deposition of ZrC layers", PhD, University of Pretoria, 2017.

[50] B. J. Lewis, W. T. Thompson and F. C. Iglesias, "Fission Product Chemistry in Oxide Fuels", *Comprehensive Nuclear Materials*, pp. 515-546, 2012.

[51] M. Ramalingam and S. Ramakrishna, *Nanofiber composites for biomedical applications*, 1st ed. Woodhead Publisher, 2017.

CHAPTER 6: RESULTS AND DISCUSSION

In this study, the microstructural changes and the interaction of the geometrically different Ti-6Al-4V alloy substrates coated with HAp, were investigated before and after immersing them in simulated bodily fluid. Two geometrically different Ti-6Al-4V alloy substrates were deposited with HAp using air plasma spraying technique. The samples were then immersed in simulated bodily fluid for different immersion periods. The resulting structural changes were analysed using SEM, EDS and XRD. In this chapter, the experimental findings are presented and discussed. First the cylinder geometry results will be discussed, followed by the flat disk results and there after the data of the two substrates of different thicknesses will be compared and discussed.

6.1 Cylinder Substrates

6.1.1 Scanning Electron Microscopy

The surface morphology and microstructure of the coatings deposited on the cylinder geometry substrate before and after immersion were investigated using Scanning Electron Microscopy.

Figure 6.1 shows the SEM images of the HAp coated Ti6Al4V substrates before and after immersion in the SBF solution for a period of 7, 28 and 56 days. The SEM image for the as-sprayed sample is shown in figure 6.1 (a). The as-sprayed coating surface is observed to be smooth with the presence of scattered glassy regions. The spherulites formed a clump (web)-like structure (indicated by yellow markings in figure 6.1 (a)). The surface is uneven with a hill-like structure indicative of an uneven growth of crystals on the surface. Micro and macro cracks (indicated by red arrows in figure 6.1 (a)) are evident together with some partially molten splats on the surface. Cracks are

present due to the high residual stress present on the surface caused by quenching stress. There are voids (indicated by blue lines in figure 6.1 (a)) between the crystals observed.

After immersion of the sample in SBF for 7-days (see figure 6.1 (b)) the surface seems to have become rougher as compared to the relatively smoother surface of the as-sprayed sample. The surface is uneven with a hill-like structure indicative of an uneven dissolution of thermal products on the surface. The image indicated that the HAp coating surface has coral-liked crystals. The surface appears to be rough, porous and it contains crystals of various shapes and sizes. These crystals are randomly orientated with some crystals taking on a circular shape (indicated by green lines in figure 6.1 (b)) while others have a flake-like structure. The surface still contains a number of voids between the crystals (indicated by blue lines in figure 6.1(b)). Cracks are yet still present on the surface (indicated by red lines in figure 6.1(b)

The SEM image of the sample immersed in SBF for 28-days is displayed in figure 6.1 (c). Immersion in SBF for 28-days resulted in the formation of clusters (indicated by yellow markings in figure 6.1 (c)), a dune like layer, some macro cracks (indicated by red markings in figure 6.1 (c)), grain boundaries and needle-like fibres on the near surface. This layer is made of spherulites and small crystals which indicates that the nucleation rate is high [1]. The probe would be in the precipitate layer therefore displaying mainly the precipitate layer on the micrograph.

After immersion for 56-days (figure 6.1 (d)), the surface is mostly covered with a continuous precipitate layer. The layer takes form of a hill-like structure with no visible voids. The micro-cracks (indicated by red markings in figure 6.1 (d)) are still present. The macro cracks on the surface are indicative of the residual stresses on the coating of the material due to thermal stress. The SEM results indicate that the immersion does have a role in changing the HAp structure.

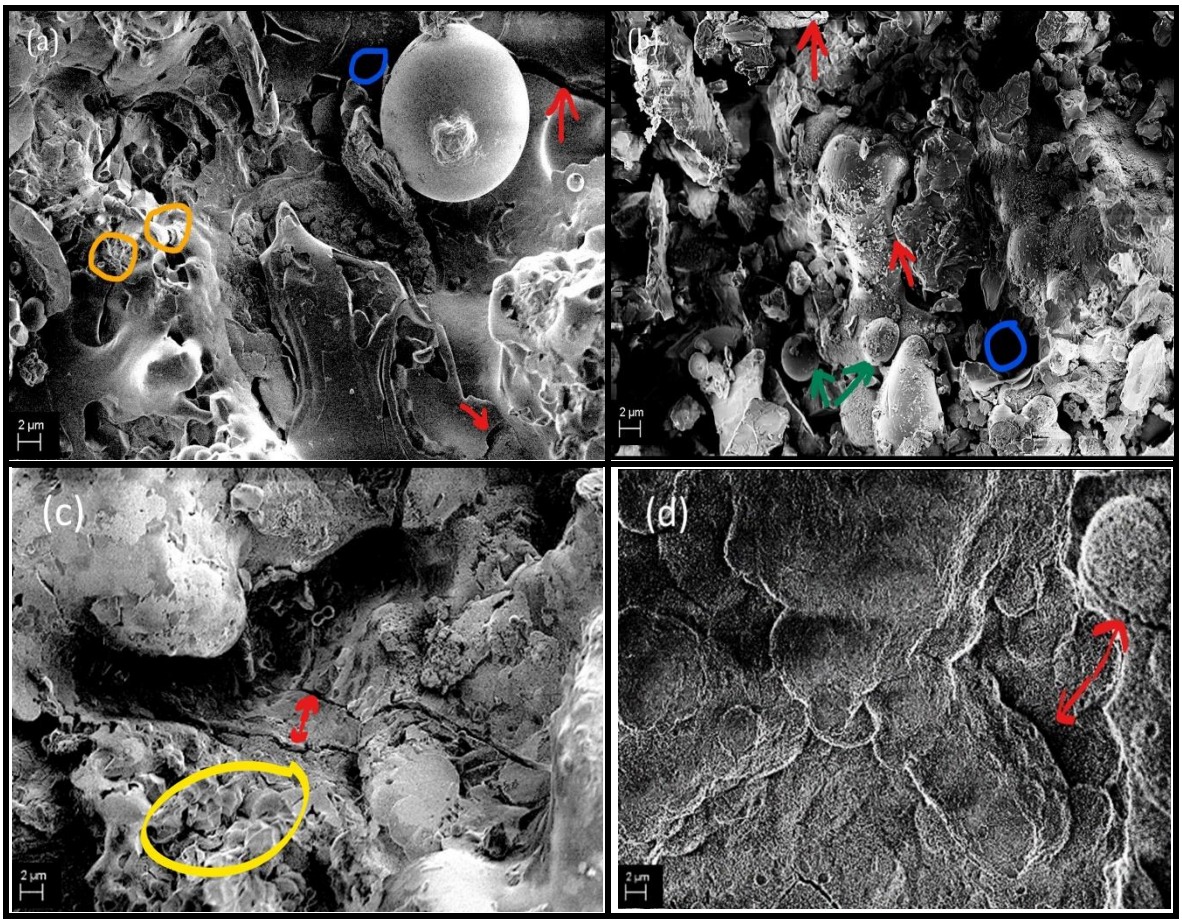

Figure 6.1*: Scanning electron micrographs of HAp coating surface for the cylinder geometry indicating morphology variation with immersion time: (a) as sprayed, (b) 7 days, (c) 28 days and (d) 56 days.*

6.1.2 Energy Dispersive X-ray Spectroscopy

Elemental analysis of the coating on the cylinder substrates before and after immersion was studied using energy dispersive X-ray spectroscopy. The cylinder samples demonstrate the dominance of calcium and oxygen from the initial stages. The as-sprayed samples show that the Ca and O is similar in wt% with the Ca being only slightly higher. After 7 days of immersion in SBF the Ca wt% decreased from 41.4 wt% to 36.9 wt% with the O increasing considerably from 41.2 wt% to 45.3 wt%. These changes are due to the sample interacting with the SBF. The phosphorous also increased slightly from 17.4 wt% to 17.9 wt%. Furthermore, analysis of the samples after immersion in SBF for 28 days indicates a presence of magnesium and sodium. Magnesium and sodium appeared after immersion with the SBF. This is due to the

sample interacting with SBF and since the probe would be in the precipitate layer therefore displaying a presence of these elements. This was also reported by other authors however their concentration is negligible as it was very small [2]. The O and Ca decreased only slightly while the P increased from 17.9 wt% to 18.3 wt%. This difference could possibly be attributed to an error when analysing due to the small difference. The samples, after immersion for 56 days, display a great decrease in the weight percentage of Ca and P while O increased considerably. The overall trend of Ca and P is that it decreased with immersion time while O increased. The weight percentage of phosphorous and calcium decrease with immersion time due to nucleation taking place on the coating while the oxygen increased as a result.

The change in the chemical composition of the samples after immersion in the SBF for varying periods of time is supported by the structural changes on the surface of the substrates as observed in the SEM images. Thus, the results observed for EDS confirm that immersion in SBF does indeed alter the structure of HAp.

Table 6.1*: Elemental composition of the HAp coating surface for the cylinder samples immersed in SBF for various periods.*

	Weight percentage (wt%)			
Element	**As sprayed**	**7 days**	**28 days**	**56 days**
Ca	41.4	36.9	36.3	17.2
O	41.2	45.3	44.7	63.4
P	17.4	17.9	18.3	17.4
Mg	0.0	0.0	0.4	0.9
Na	0.0	0.0	0.3	1,1
Total	100	100	100	100

6.1.3 X-ray Diffraction

XRD was used to determine the structural changes and the thermal products formed on the coating of the samples before and after immersion into the SBF.

6.1.3.1 Phase Identification

Figure 6.2 shows the diffraction pattern for the as-sprayed cylinder geometry substrate together with that of HAp powder. The as-sprayed diffraction pattern contains peaks which belong to the diffraction pattern of the main HAp phase together-with 3 additional peaks. These additional peaks are at the 2θ position of 29°, 31° and 37.5°. These peaks are a result of the thermal products forming on the coating surface due to thermal decomposition of the starting HAp powder upon exposure to the plasma [3]. The peaks at 29°, 31° and 37.5° belong to tricalcium phosphate (TCP), tetracalcium phosphate (TTCP) and calcium oxide (CaO), respectively. These peaks were also reported in the findings by other research groups [3]. The intensity of all the HAp peaks on the as-sprayed sample diffraction pattern appears to be lower than the intensity of the peaks on the HAp powder diffraction pattern indicating that the coatings on the samples contain an amount of amorphous content.

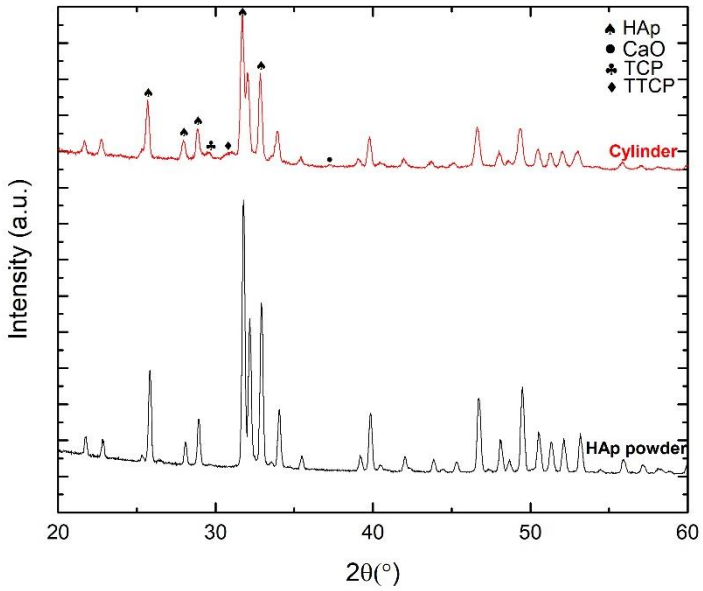

Figure 6.2: *XRD pattern of starting HAp powder superimposed with the as-sprayed diffraction patterns for cylinder geometry substrates.*

Figure 6.3 shows the XRD patterns of HAp coatings deposited on the cylinder geometry substrates, immersed in SBF for varying time periods. The HAp is observed to be the dominant phase for all immersion periods. The HAp peak intensity increases after immersion in the SBF and thereafter continues to increase with immersion time. The peak at 37.5° 2θ, corresponding to the thermal product CaO, ceases to exist after 7 days indicating that the phase disappears within 7 days of immersion in SBF. The intensities of the peaks at 2θ positions of 29° and 31°, corresponding to TCP and TTCP respectively, decrease after immersion indicating a decrease of these phases. Hence the TCP and TTCP dissolve throughout the immersion period. The increase in peak width for the HAp peaks observed on coatings immersed for 28 and 56 days is attributed to the nano particles in the precipitate.

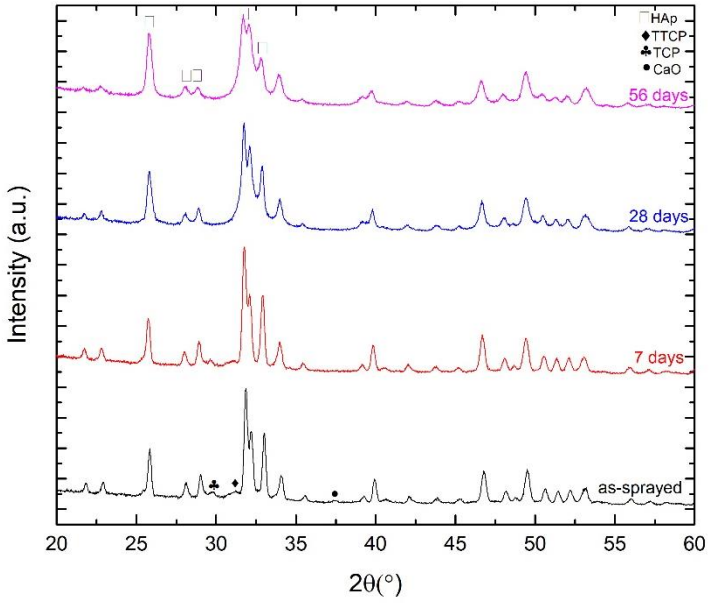

Figure 6.3: *XRD patterns of the near surface regions of the as-sprayed and immersed samples for the cylinder substrates.*

XRD quantitative phase analysis (QPA) using Rietveld refinement was then done on the coatings for all immersion periods using the data in figure 6.3. The figure 6.4 displays a representative Rietveld refinement for HAp coatings used for quantitative phase analysis with the quality fit shown by the curve at the bottom. This curve is known as the difference curve. The difference curve is the difference between the measured and the calculated diffraction patterns. For a perfect fit, the difference curve is a straight line.

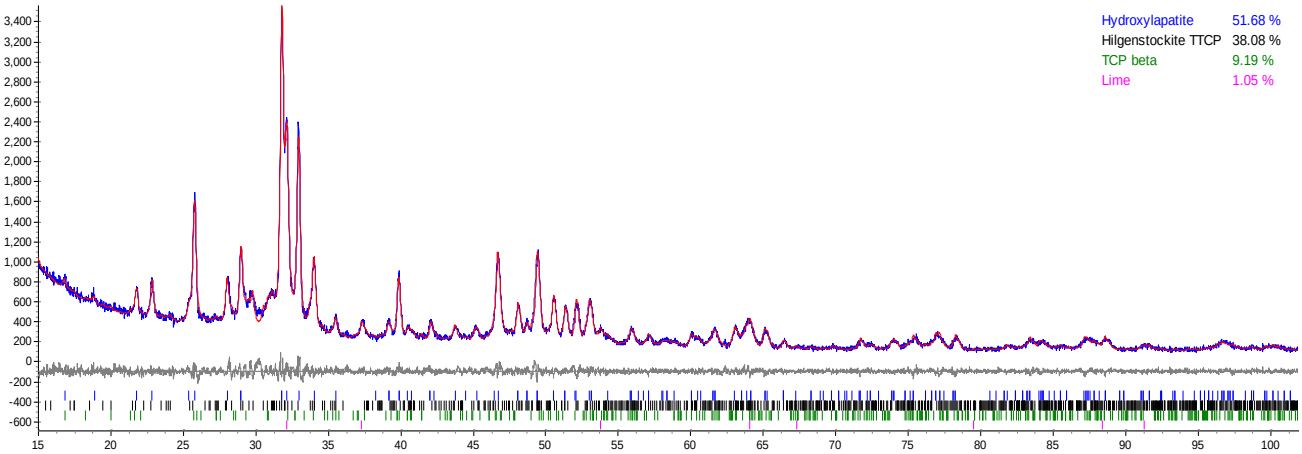

Figure 6.4: *Rietveld refinement for HAp coating for QPA.*

The results for the XRD QPA is shown in figure 6.5. The HAp phase in the cylinder geometry substrate increases from 77.24 wt% to 82.61 wt% after 7 days of immersion and thereafter increases slightly and eventually stabilizes around 83.97 wt% after 56 days of immersion. The HAp phase in the cylinder substrate is already high and increases only slightly by 7% within 7 days of immersion. Nimkerdphol also observed the HAp to have increased in the first 7 days after immersion [4]. Within 7 days of immersion, the CaO disappears immediately while the thermal product TTCP decreased from 17.61 wt% to 9.30 wt%, a drastic reduction of 47.20%. The TCP phase initially decreases slightly after 7 days of immersion by 17.44% from 4.76 wt% to 3.93 wt% and thereafter increases eventually reaching 6.67 wt% after 56 days of immersion.

During the first 7 days of immersion the CaO disappears immediately, and the HAp phase increases while the thermal products TCP and TTCP decrease due to dissolution of Ca^{2+} and PO^{4-} ions. The dissolution of these ions from the surface coating into the SBF occurs due to the existence of an ion gradient [5]. This causes the observed results of the relative increase in the HAp phase with the decrease in the thermal products TTCP, TCP and CaO. The HAp coating that is left on the surface, after the dissolution of the ions, is more stable and crystalline since the thermal products and amorphous content formed, start to disappear. Thereafter there is a slight increase observed for the HAp phase with a slight increase in the TCP and decrease in the TTCP. With further immersion, the HAp phase seems to show a slight increase.

It is clear from the XRD results obtained that there are changes in the composition after immersion of the samples in the SBF. The chemical composition of HAp changes after the samples were immersed in the SBF. These changes in the HAp material were also noted in SEM and EDS which are in agreement with the results.

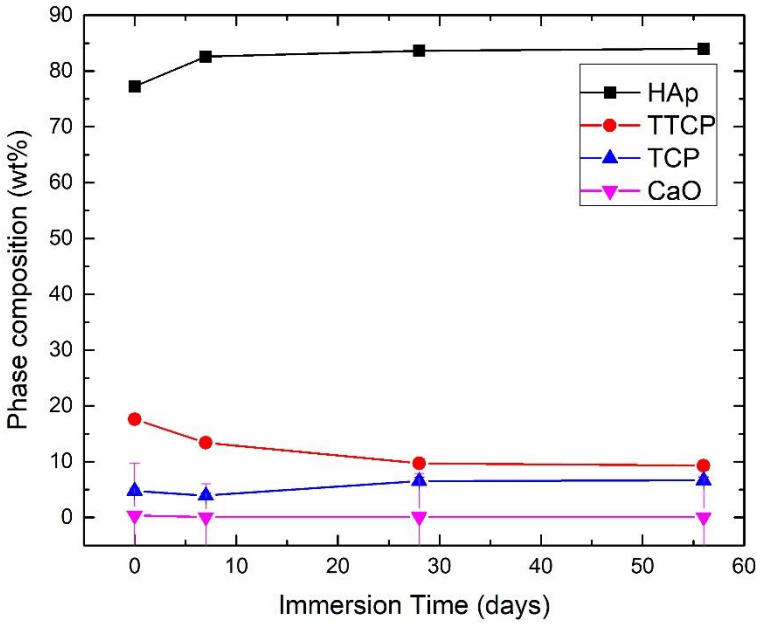

Figure 6.5: *Quantity phase analysis of the HAp and thermal products present with immersion time for the surface of the cylinder geometry substrates.*

6.1.3.2 Residual Stress

Figure 6.6 shows a typical 2-dimensional diffraction pattern of the coating collected with the Discover instrument. The inset is the corresponding 1-dimensional pattern after integration.

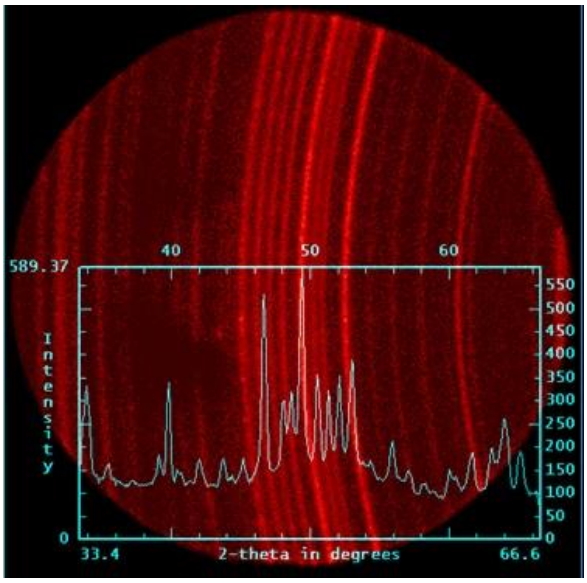

Figure 6.6: *2-dimensional diffraction pattern of coating (inset is the corresponding 1-dimensional pattern).*

The residual stresses which were calculated using HAp213 reflections (~49° in 2θ), of the coatings deposited on the cylinder substrates were obtained and are shown in table A1 (Appendix A). Averages of the normal stresses measured at different points and of individual normal stresses i.e. σ_{11} and σ_{22} are summarized in table 6.2. The normal stresses in the coating are shown to be tensile for all immersion periods.

Table 6.2: *Average residual stresses on the surface of the coating deposited on cylinder substrates for various immersion periods.*

Immersion period	**Data points average (MPa)**		**Normal stresses average (MPa)**
	σ_{11}	**σ_{22}**	
As-sprayed	54.04 ± 1.51	54.65 ± 2.24	54.35 ± 0.31
7 days	53.82 ± 2.89	48.94 ± 4.17	51.38 ± 2.44
28 days	44.17 ± 2.00	39.97 ± 1.94	42.07 ± 2.10
56 days	39.15 ± 2.85	31.98 ± 2.25	35.57 ± 3.59

The stresses present on the surface after coating are tensile possibly due to the superposed contribution from the three different types of stresses namely, quenching stress, thermal stress and phase transformation stress. The average normal stresses, σ_{11} and $\sigma_{22,}$ for the as-sprayed sample are 54.04 MPa and 54.65 MPa, respectively. Quenching stress is described in the theory of stress (Experimental Procedure). The corresponding stresses generated in the coating are therefore quenching stresses. Thermal stresses are also described in the theory of stress (Experimental Procedure) however, given the thickness of the coating in relation to that of the substrate, thermal stresses are considered negligible.

After 7 days of immersion, the average of the normal stresses decreases from 54.35 MPa to 51.39 MPa. When the stress exceeds the ultimate tensile stress (UTS) of 38.0 – 48.0 MPa, it begins to decrease. The coating relieves the extra stress by cracking and causing the cracks to become longer with immersion time as observed on the SEM

images. The decrease of the normal stresses can also be due to the amorphous content and thermal products dissolving in the SBF after immersion. This could cause a rearrangement of stress on the surface. After immersion in the SBF for 7 days the apatite layer also begins nucleating. The stresses thereafter decrease after 28 days of immersion to 42.07 MPa and ultimately to 35.57 MPa after 56 days of immersion. As the sample is immersed longer in the SBF, the precipitate layer continues to grow. This happens since the thermal products dissolve into the fluid while the substrate is immersed, and this causes the stress present in the coating to rearrange itself to the more later formed coating. After the stress on the coating exceeds its UTS, the stress begins to decrease due to cracks. The normal stress in the cylinder substrates were observed to decrease within immersion time. The shear components, $\sigma_{ij's}$ are negligible, not exceeding 12 MPa therefore not reported.

6.2 Flat Disk Substrates

6.2.1 Scanning Electron Microscopy

Figure 6.7 displays the SEM images of the HAp coated Ti-6Al-4V alloy flat disk substrates before and after immersion in the SBF. The SEM image of the as-sprayed sample is shown in figure 6.7 (a). The surface appears to be quite porous containing voids (indicated by blue markings in figure 6.7 (a)) and glassy regions. The glassy regions arise from the individual molten splats spreading out, upon impact on the substrate, to form regions containing smooth edges. It can be seen that partially molten particles are present on the surface. This occurs since some large particles didn't melt or have partially melted when they exit the plasma jet. There appears to be spherulites of different sizes present on the surface with some spherulites joining together. There is small agglomeration (indicated by yellow markings in figure 6.7 (a)) of the spherulites which is spreading across the surface. Microcracks (indicated by red lines in figure 6.7 (a)) are evident on the surface, which are indicative of high residual stress

arising due to quenching and thermal stresses attributed to the mismatch in thermal expansion of the coating and the substrate [1].

The surface morphology of the sample immersed in SBF for 7-days is shown in figure 6.7 (b). Immersion of the sample in SBF for 7-days, showed a porous (indicated by blue markings in figure 6.7 (b)) microstructure of HAp and some clusters (indicated by yellow lines in figure 6.7 (b)). The surface appears to contain some glassy regions. The cracks are now wider and longer. The partially molten splats are still present and most of the spherulites have grouped together.

The SEM image of the sample immersed in SBF for 28-days is shown in figure 6.7 (c). The micrograph shows the formation of spherulites and the agglomeration of crystals forming a precipitate/apatite layer (indicated by orange arrows in figure 6.7 (c)). This apatite layer appears to cover most of the surface coating leaving a few voids. There is still evidence of cracks together with needle-like fibres (indicated by pink markings in figure 6.7 (c)) covering the surface. Micro-cracks indicative of residual stress present in the coating of the surface due to thermal stress.

The surface morphology for the sample, after immersion in SBF for 56-days, is shown in figure 6.7 (d). The apatite layer seems to cover the entire surface now, leaving just small pores (indicated by blue markings in figure 6.7 (d)) present with a surface that is much smoother after immersion for 56 days. The needle-like fibres (indicated by pink markings in figure 6.7 (d)) appear to be more spaced out and the cracks now appear narrower which could be due to the precipitate layer covering majority of the surface. There still appears to be some porous regions present.

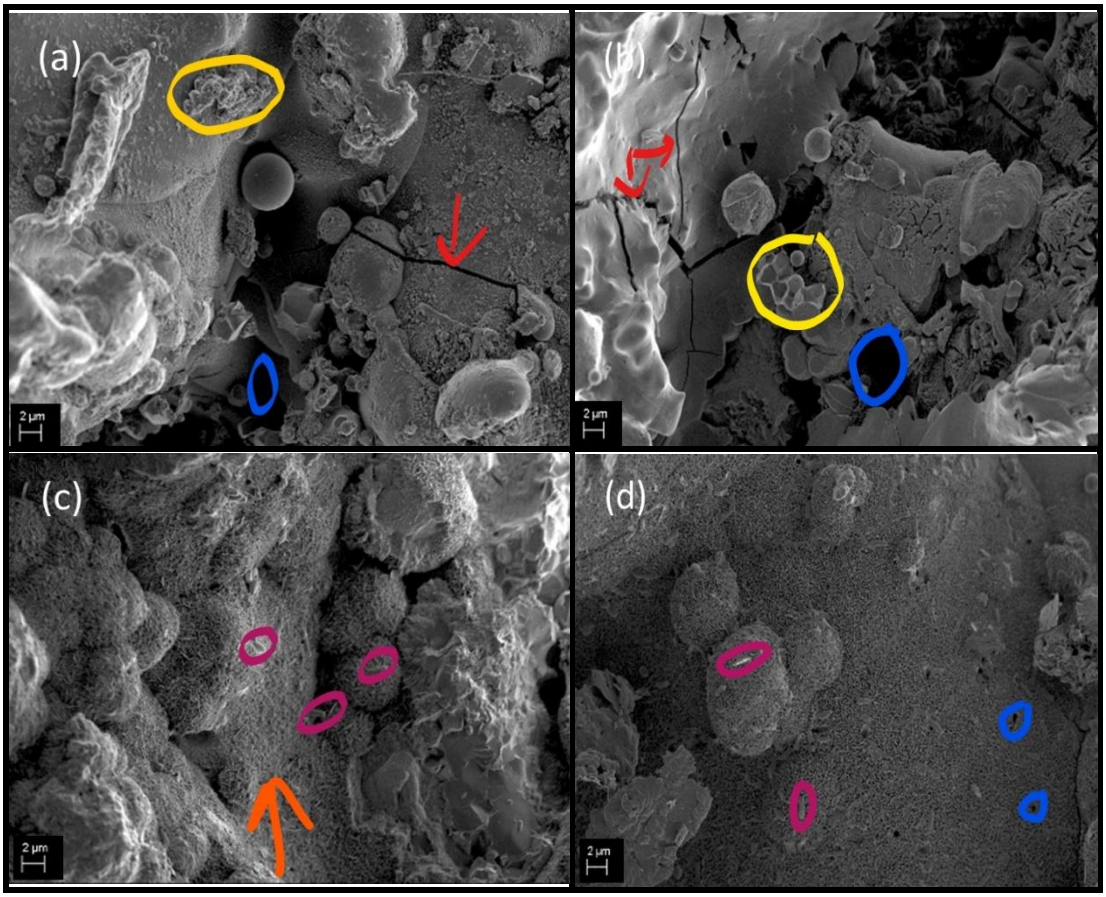

Figure 6.7: *Scanning electron micrographs of HAp coating surface for flat disk geometry indicating morphology variation with immersion time: (a) as sprayed, (b) 7 days, (c) 28 days and (d) 56 days.*

6.2.2 Energy Dispersive X-ray Spectroscopy

Elemental analysis of the coating on the flat disks substrates before and after immersion was studied using energy dispersive X-ray spectroscopy. The flat disks demonstrate the dominance of calcium and oxygen from as-sprayed samples. The as-sprayed samples show that the Ca and O have a weight percentage which is quite similar. There is also a 16.3 wt% of P present with a very small amount of Si as well. After 7 days of immersion in SBF the Ca wt% increased from 40.5 wt% to 44.2 wt% with the O decreasing considerably from 42.4 wt% to 36.83 wt%. The phosphorous also increased slightly from 16.3 wt% to 18.4 wt%. However, analysis of the samples after immersion in SBF for 28 days indicates a presence of magnesium, sodium and chlorine. The magnesium,

sodium and chlorine are present in the top layer after immersion with the SBF and since the probe would be in the precipitate layer it would therefore show a presence of these elements. Mg and Na were also observed by Bharati et al. [2]. The Ca wt% now decreased to 39.9 wt% while the O and P increased to 39.5 wt% and 18.8 wt%, respectively. The samples, after immersion for 56 days, display a great decrease in the weight percentage of Ca and P while O increased considerably. The weight percentage of phosphorous and calcium decrease with immersion time due to precipitation of the Ca and P ions taking place on the coating while the oxygen increased as a result. The Mg and Na wt%, after 56 days of immersion in the SBF, remained the same however a 0.2 wt% of Al was found.

The change in the chemical composition of the samples after immersion in the SBF for varying periods of time are supported by the structural changes on the surface of the substrates as observed in the SEM images. Therefore, the results observed for EDS confirm that immersion in SBF does indeed alter the structure of HAp.

Table 6.3*: Elemental composition of the HAp coating surface for the flat disks immersed in SBF for various periods.*

	Weight percentage (wt%)			
Element	**As sprayed**	**7 days**	**28 days**	**56 days**
Ca	40.5	44.2	39.9	35.9
O	42.4	36.8	39.5	43.8
P	16.3	18.4	18.8	18.3
Si	0.3	0.3	0.0	0.0
Mg	0.0	0.0	0.7	0.7
Na	0.0	0.0	0.8	0.8
Cl	0.0	0.0	0.3	0.3
Al	0.0	0.0	0.0	0.2
Total	100	100	100	100

6.2.3 X-ray Diffraction

XRD was used to determine the structural changes, phase composition and residual stress on the coating of the samples before and after immersion into the SBF.

6.2.3.1 Phase Identification

Figure 6.8 shows the as-sprayed diffraction pattern for the flat disk superimposed with that of the HAp powder. As with the cylinder, the as-sprayed diffraction pattern contains peaks, which belong to the diffraction pattern of the starting HAp phase together with 3 additional peaks. These additional peaks are at the 2θ position of 29°, 31° and 37.5° and belong to tricalcium phosphate (TCP), tetracalcium phosphate (TTCP) and calcium oxide (CaO), respectively. The intensity of all the HAp peaks on the as-sprayed sample diffraction pattern appears to be lower than the intensity of the peaks on the HAp powder diffraction pattern indicating that the coatings probably contain an amount of amorphous content.

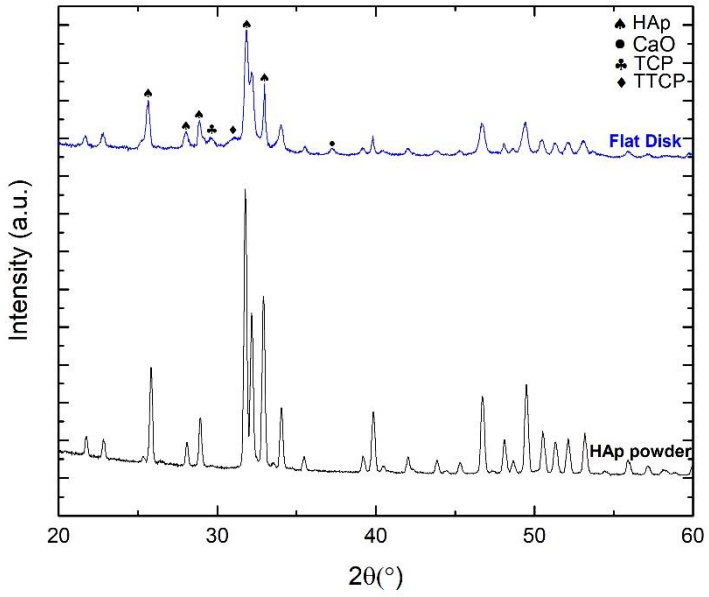

Figure 6.8: *XRD pattern of starting HAp powder superimposed with the as-sprayed diffraction patterns for the flat disk*

Figure 6.9 shows the XRD patterns of the flat disk samples, immersed in SBF for varying time periods. The HAp is the dominant phase for all immersion periods. The HAp peak intensity increases after immersion in the SBF for 7 days and thereafter continues to increase with immersion time. The peak at 37.5° disappears after 7 days indicating that the thermal product CaO disappears within this period of immersion in SBF. The peak intensities of the peaks at 2θ positions of 29° and 31° decrease drastically. Thereafter it appears to continue decreasing with increasing immersion time in the SBF. Therefore, the TCP and TTCP dissolve throughout the immersion period. The increase in peak width observed on coatings immersed for 28 and 56 days is attributed to the nano particles in the precipitate.

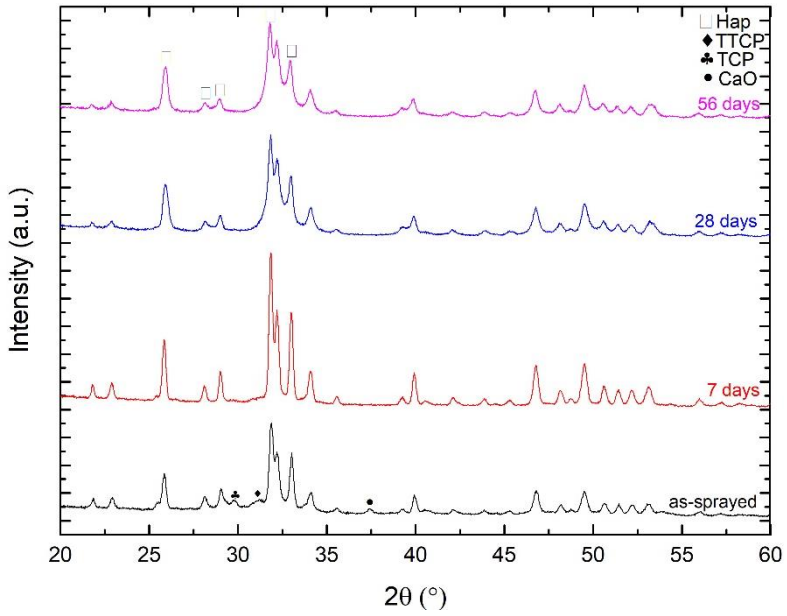

Figure 6.9: *XRD patterns of the near surface region of the as-sprayed and immersed samples for the flat disk substrates.*

XRD quantitative phase analysis was then done on the coatings using Rietveld refinement for all immersion periods. XRD patterns shown in figure 6.10 was used for quantitative analysis. The HAp phase in the flat disks increases from 70.44 wt% to 87.67 wt% (24.46%) after 7 days of immersion and thereafter slowly decreases and eventually stabilizing around 83.35 wt% after 56 days of immersion. The change in HAp within 7

days of immersion is large therefore immersion caused a significant increase in the HAp phase. Nimkerdphol [4] also observed the HAp to have increased in the first 7 days after immersion. During this period, the CaO disappears while the thermal products TTCP and TCP decrease from 22.92 wt% and 5.06 wt% to 8.26 wt% (64%) and 3.82 wt% (24.50%) respectively. The TTCP decreases by a large amount within 7 days of immersion. Thereafter the TTCP and TCP increase slightly with immersion time to 10.43 wt% and 6.23 wt% (small increases), respectively, stabilizing with further immersion.

It was observed during the first 7 days of immersion that the CaO disappears immediately, and the HAp phase increases while the thermal products TCP and TTCP decrease. The disappearance of CaO and decrease of TCP and TTCP occurs due to the dissolution of Ca^{2+} and PO^{4-} ions. As indicated, the dissolution of Ca^{2+} and PO^{4-} from the coating surface into the SBF occurs due to the existence of an ion gradient [5]. This causes the observed increase in the HAp phase with the decrease in the thermal products TTCP, TCP and CaO. The HAp coating that is left on the surface, after the dissolution of the ions, is found to be more stable and crystalline [3]. Thereafter there is a gradual decrease observed for the HAp phase with immersion with a slight increase in the TCP and TTCP. With further immersion, the HAp phase shows a slight decrease which might be due to: 1) the decline of the existing ion gradient causing a decrease in dissolution or 2) supersaturation of the solution [3]. Supersaturation of the solution causes the precipitate layer to form on the surface, as can be seen on the SEM images, causing a stop in further dissolution since this layer causes a “blanketing” effect on the coating.

The changes in the HAp materials observed in XRD results are in agreement with the SEM and EDS data reported earlier in this dissertation. It is clear that the immersion in SBF causes the EDS crystal and composition to change.

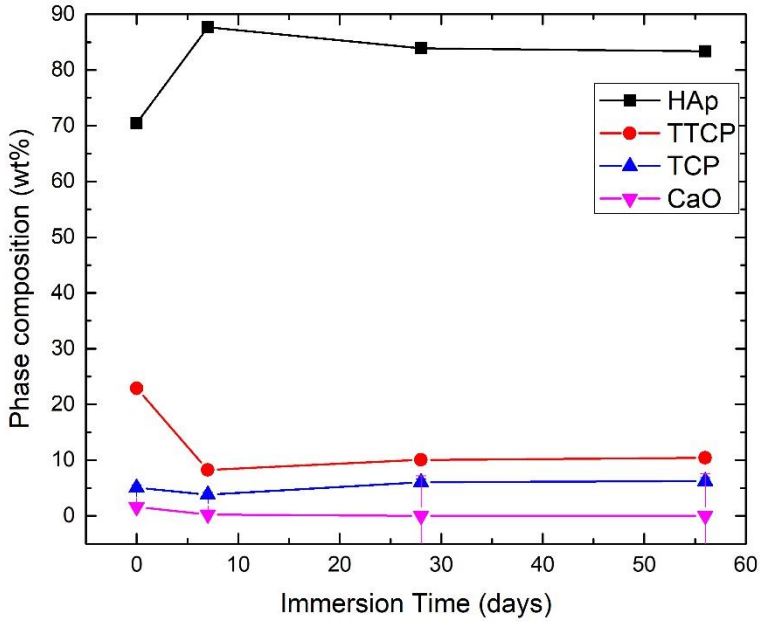

Figure 6.10: *Quantity phase analysis of the HAp and thermal products present with immersion time for the flat disk substrates.*

6.2.3.2 Residual Stress

The residual stresses of the coatings deposited on the flat disk substrates were obtained and are shown in table A2 (Appendix A) and the averages of the normal stresses measured at various points and of individual normal stresses i.e., σ_{11} and σ_{22} are summarized in table 6.4. As with the cylinder the normal stresses in the coating are shown to be tensile.

Table 6.4: *Average residual stresses on the surface of the coating deposited on flat disk substrates for various immersion periods.*

Immersion period	**Data points average (MPa)**		**Normal stresses average (MPa)**
	σ_{11}	**σ_{22}**	
As-sprayed	36.78 ± 1.31	38.66 ± 2.19	37.72 ± 0.94
7 days	43.66 ± 3.21	36.53 ± 3.39	40.10 ± 3.57
28 days	30.91 ± 1.04	30.67 ± 1.47	30.79 ± 0.12
56 days	31.52 ± 3.06	27.61 ± 2.53	29.57 ± 1.96

For the flat disk substrates, the average normal stresses, σ_{11} and σ_{22}, for the as-sprayed sample are 36.78 MPa and 38.66 MPa respectively due to quenching stress. After 7 days of immersion, the average of the normal stress components increased from 37.72 MPa to 40.10 MPa. The increase of the normal stresses can be due to the amorphous content and thermal products dissolving in the SBF. This could cause a rearrangement of stress on the coating therefore generating phase transformation stress. After immersion in the SBF for 7 days the apatite/precipitate also begins nucleating. There was however a decrease to 30.79 MPa after the samples were immersed for 28 days. With further immersion i.e., 56 days, the normal stresses decreased slightly to 29.57 MPa. There is an initial residual stress in the HAp coating due to air plasma spraying the powder on the surface of the substrate. This mechanism was explained in the theory of stress (Experimental Procedure) and appeared to be the case for the cylinder geometry substrates as well. The decrease with further immersion could be attributed to cracking observed on the coating surface as a result of the stress exceeding the UTS.

The trend of the stress in the coatings observed mirror the trend of the HAp wt% from the XRD quantitative phase analysis for the flat disk substrates. It is clear that the immersion in SBF causes a change in the structure of the surface of the substrates.

6.3 Comparison

Scanning electron microscopy was done on both substrate geometries to analyse the surface morphology of the samples. The as-sprayed coating on cylinder substrates were observed to have more crystals of various shapes whereas the flat disk substrates contain more spherical particles. This could be due to a greater amount of stress on the cylinder samples. The flat disks appear with more cracks and the cylinder substrates have more voids present. After immersion in the SBF for 7 days both the substrates have an increase in the roughness on the surface. More cracks are present, and the crystals and spherulites have clumped together. After immersion in SBF for 28 days, the samples

show an apatite layer appearing to form that covers most of the surface leaving a few voids present. Both substrate geometries are mostly covered with the Ca-P apatite later after 56 days of immersion and the number of cracks had increased. Therefore, the thickness of the substrate does not have an effect on the growth of the apatite layer.

Elemental analysis of the coating on the substrates before and after immersion was studied using energy dispersive X-ray spectroscopy. Both samples demonstrate the dominance of calcium, oxygen and phosphorous with the weight percentage of oxygen found to be much lower in the flat disk geometry than that of the cylinder geometry. The weight percentage of the calcium in the flat disks appears to have increased after immersion for 7 days in the SBF and thereafter appears to decrease further with immersion. The cylinder samples however appear to have calcium decreasing in weight percentage since immersion in SBF for 7 days. After 56 days of immersion, the flat disks appeared to have aluminium, silicone and chlorine present however this was not found in the coating deposited on cylinder geometry substrates. This difference could be attributed to a difference in stress on the top surface layer of the samples. From table 6.1 and 6.3 it follows that both sample geometries, after immersion for 56 days, display a decrease (albeit very small) in the weight percentage of P while O increased considerably. The weight percentage of phosphorous and calcium decrease with immersion time due to nucleation and precipitation taking place on the surface of the coating while the oxygen increased as a result. The change in composition after immersion was evident by the changes in the surface morphology as seen in the SEM images.

XRD was used to determine the structural changes and the thermal products formed on the coating of both sample geometries before and after immersion into the SBF. The HAp peaks of the cylinder coated sample appear to have a higher intensity than the HAp peaks of the flat disk samples for the as-sprayed sample. The peaks of the thermal products thus appear to have a lower intensity for the cylinder samples as a result of the high HAp peaks. This could be due to the cylinder samples having more volume for

thermal diffusion to take place. The cylinder therefore acts as a 'heat sink' thus allowing the top flat surface to be cooler than the surface of the flat disks.

XRD quantity phase analysis was then done on both substrate geometries for all immersion periods. Figure 6.11 displays the quantitative phase analysis for the cylinder geometry substrates superimposed with that of the flat disk substrates. Both samples displayed HAp being the dominant phase after air-plasma spraying. The HAp phase was found to increase after 7 days of immersion by 7% and 24.46% for the cylinder substrates and flat disks, respectively. The initial HAp phase was greater in the cylinder substrates and increased only slightly within 7 days of immersion as compared to the flat disks. Thereafter the HAp phase for the cylinder geometry substrates stabilizes with further immersion while decreasing slightly for the flat disk substrates before stabilizing. The thermal product CaO, in both geometries, disappears within 7 days of immersion while the TTCP and TCP decrease. The TTCP decreases by 47.20% and 64% for the cylinder substrates and flat disks, respectively and the TCP decreases by 17.44% and 24.50% for the cylinder substrates and flat disks, respectively. Since the flat disks contained a higher amount of thermal products initially, there is more TCP and TTCP to dissolve in the SBF therefore the thermal products decrease by a greater percent after immersion. The TCP thereafter increased (slight increase) with immersion time for both sample geometries. However, the TTCP decreased and increased for the cylinder and flat disk geometry substrates, respectively within 28 days of immersion and thereafter was found to stabilize. The TCP and TTCP were observed to eventually stabilize within 56 days of immersion at approximately the same wt % for both geometries. After 28 days of immersion both the substrate geometries were observed to have the same weight percentage, within error margins, for all the phases.

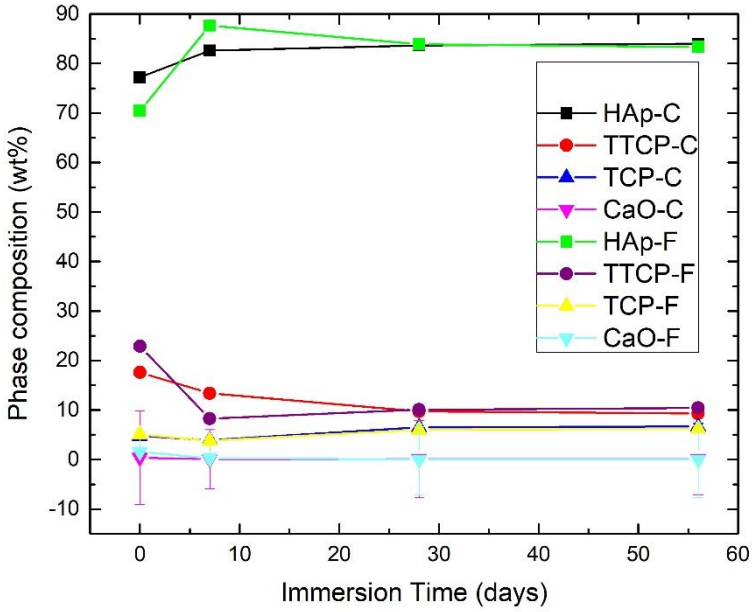

Figure 6.11: *Quantity phase analysis of the HAp and thermal products present with immersion time for the for both geometries.*

Figure 6.12 shows the normal stresses of the coating deposited on both substrate geometries for all immersion times. As indicated in figure 5.9 (of experimental procedure), the stresses were determined at various points across the coating surface. For each immersion period, with the exception of 56 days for the disk sample, two samples collected from the same batch were analysed. The cylinder samples appear to have normal stresses higher than that of the flat disk substrates. This slightly higher stress observed in the as sprayed cylinder could be attributed to the larger amount of quenching and thermal stresses due to rapid quenching and difference in CTE. Due to the high amount of heat required to raise the temperature of the cylinder volume to that of the disk it will therefore take slightly longer to heat up the surface of the cylinder to the same temperature as that of the flat disk substrates. The incoming HAp droplets therefore experience more pronounce quenching effects and for a period slightly longer for the cylinder as compared to the disk. With quenching stresses proportional to ΔT, as per equation (5.7) (Experimental Procedure) the expected residual stress will therefore be higher in the cylinder.

After 7 days of immersion the stress for the flat disk substrates increased while the stress for the cylinder substrates decreased as it has already exceeded its UTS. In figure 6.12 (b) the points for both geometries appear very scattered. This can be attributed to the relatively higher surface roughness as a results dissolution occurring at the coating surface together with the onset of apatite nucleation. The different regions of the surface are therefore affected differently. With further immersion (28 days), both the substrates appear to have a decrease in the average normal stress. In figure 6.12 (c) the scattering between points is smaller and therefore the plot is observed smoother as compared to the previous figure. This smoother plot is due to the precipitate layer starting to cover most of the surface. After 56 days of immersion both substrates displayed a decrease in the average stress. The figure 6.12 (d) is observed smoother now as the precipitate layer covered the coating surface completely. These plots are in agreement with the surfaces observed in the SEM images.

Overall, the normal stresses, σ_{11} and $\sigma_{22,}$ are both greater in magnitude for the cylinder geometry substrates as compared to the flat disk substrates for all immersion periods. Although it would seem that air plasma spraying is not ideal to coat thick substrates or large components due to the larger residual stresses (as shown large cracks present on the surface) generated, the problem can be mitigated by raising the temperature of the thick substrate prior to deposition. This will reduce the temperature difference between the substrate and HAp droplet hence minimizing the quenching effect. Within the error margin, the normal residual stresses appear homogenous throughout the coating surface with a few outliers present, this suggests that the technique produces homogenous coatings with relatively homogenous residual stress. Within the error margins, normal stresses of samples collected from the same batch seem to agree therefore suggesting that the technique can be used to coat multiple substrates with a reasonable degree of reproducibility.

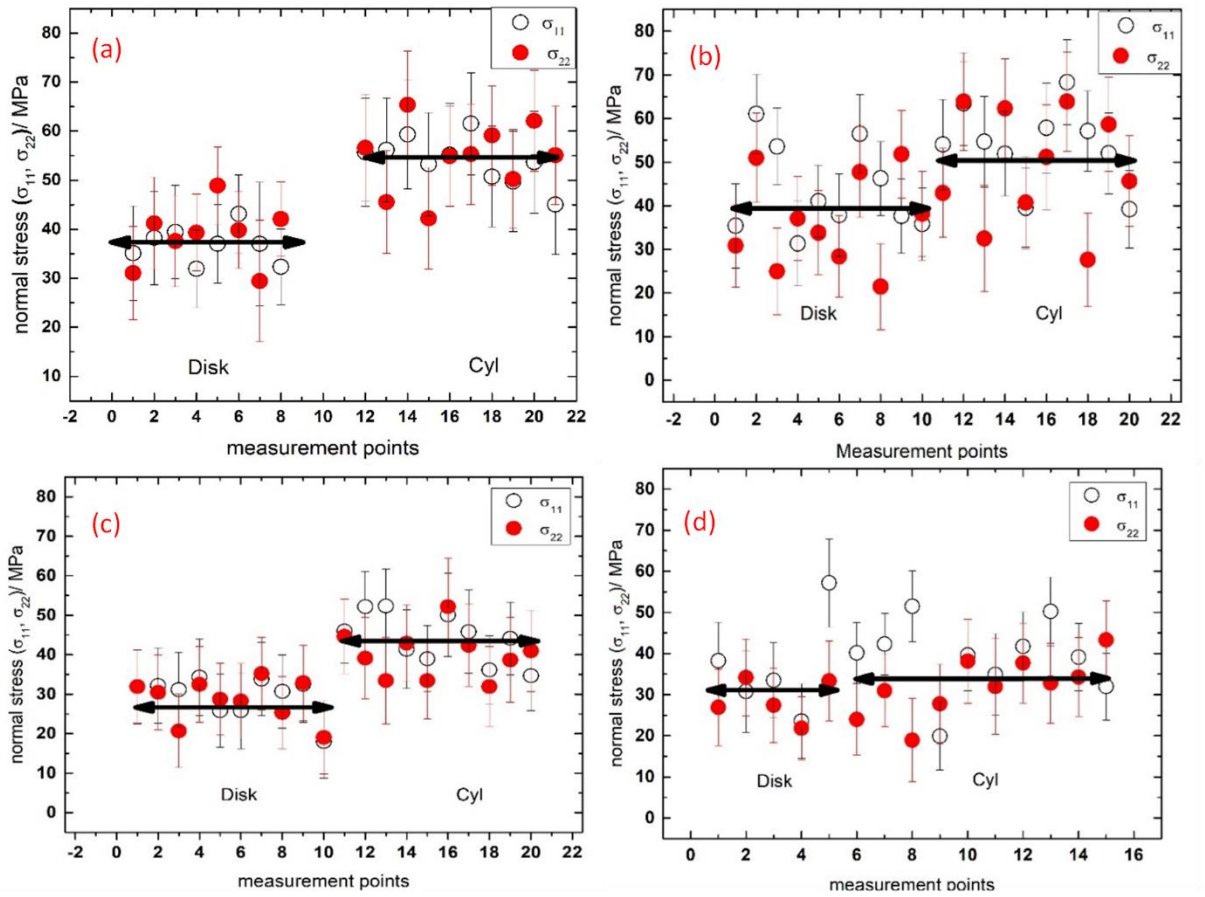

Figure 6.12: *Normal stresses σ_{11} and σ_{22} collected at different measurement periods for various immersion periods: (a) as-sprayed, (b) 7 days, (c) 28 days and (d) 56 days (The solid line through the points is a guide to the eye).*

Figure 6.13 shows the average of the normal stresses, σ_{11} and σ_{22} of the coating deposited on both substrate geometries. It can be seen in figure 6.13 that the cylinder substrates appear to show a linear behaviour with the stress decreasing from ~55 MPa for as-sprayed to ~35 MPa after 56 days of immersion in the SBF. However, for the flat disk substrates, after immersion in the SBF for 7 days the stress increases and thereafter decreases after immersion for 28 days. As stated above, the increase after 7 days of immersion can be due to the amorphous content and thermal products dissolving in the SBF causing a rearrangement of stress on the surface. During this period, the apatite layer also begins nucleating which contributes to the different in the stress. After 56 days of immersion, the average stress for both substrate geometries decreased but only

slightly for the flat disk substrates. Eventually both of the substrates reached a very similar average stress after 56 days of immersion. The stress for the cylinder substrates is initially higher before immersion and remains higher up until immersion for 56 days. However, the difference of the stress between the two geometries decreased with immersion time. Within error margins, the stress for the cylinder substrates is equal to the stress for the flat disks after 56 days of immersion, as observed in the figure 6.13. This could be attributed to the fact that after 56 days immersion, the penetration depth of the X-rays could be similar to the thickness of the precipitate layer therefore majority of the scattered signal comes from the newly formed apatite layer.

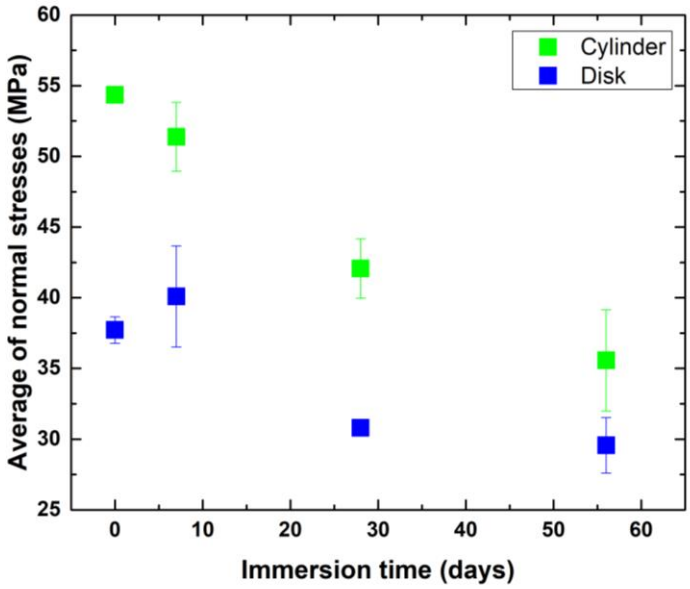

Figure 6.13: *Average of normal stresses σ_{11} and σ_{22} for various immersion periods for both geometries: cylinder and flat disk substrates.*

6.4 References

[1] Y. W. Gu, K. A. Khor and P. Cheang, "In vitro studies of plasma-sprayed hydroxyapatite/Ti-6Al-4V composite coatings in simulated body fluid (SBF)", *Biomaterials*, vol. 24, no. 9, pp. 1603-1611, 2003.

[2] S. Bharati, M. K. Sinha and D. Basu, "Hydroxyapatite coating by biomimetic method on titanium alloy using concentrated SBF", *Bulletin of Materials Science*, vol. 28, no. 6, pp. 617-621, 2005.

[3] T. P. Ntsoane, "In-vitro investigation of air-plasma sprayed hydroxyapatite coatings deposited on two geometrically different substrates", PhD, University of Pretoria, 2020.

[4] A. Rakngarm Nimkerdphol, Y. Otsuka and Y. Mutoh, "Effect of dissolution/precipitation on the residual stress redistribution of plasma-sprayed hydroxyapatite coating on titanium substrate in simulated body fluid (SBF)", *Journal of the Mechanical Behavior of Biomedical Materials*, vol. 36, pp. 98-108, 2014.

[5] S. Radin and P. Ducheyne, "The effect of calcium phosphate ceramic composition and structure on in vitro behavior. II. Precipitation", *Journal of Biomedical Materials Research*, vol. 27, no. 1, pp. 35-45, 1993.

CHAPTER 7: CONCLUSION

7.1 Conclusion

In this study, HAp powder was deposited on the flat surface of two sets of Ti-6Al-4V substrates of different thicknesses (5mm thick flat disks and 25mm thick cylinder samples). The two sets of samples were then immersed in SBF to determine the biofunctional performance of the coatings. The two sets of geometrically different substrates were compared before and after immersion. The structural changes of the samples before and after immersion were then investigated using SEM and EDS. In addition, the microstructure and the residual stress was analysed and measured using XRD. The main aim of the investigation was to evaluate the effect of substrate thickness on the air-plasma sprayed coatings.

The results indicated that coating the HAp on the Ti-6Al-4V substrates using air plasma resulted in the presence of the thermal products namely, CaO, TCP and TTCP. These thermal products were formed in the hot plasma jet and then deposited on the substrates. These thermal products after immersion in the SBF decreased leaving the surface with more crystalline HAp since the amorphous content decreased on the surface.

The surface morphology of the samples were characterized using SEM. The as-sprayed surface for the cylinder sample was observed to have more crystals whereas the flat disk surface contained more spherical particles. This is due to the greater amount of stress present in the cylinder sample after plasma spraying. The surfaces after immersion in SBF for 7 days were rougher and the crystals agglomerated after immersion in both substrate geometries. However, after 28 days of immersion in the SBF both substrate geometries had a precipitate layer forming on the surface of the substrate. After 56 days of immersion the surfaces were fully covered with the precipitate layer leaving no visible voids.

EDS analysis of the substrate geometries displayed the dominance of Ca and O for both samples. The cylinder samples were observed to have the weight percentage of calcium decreasing from immersion in the SBF for 7 days. However, the flat disk samples observed an increase in the weight percentage of calcium after 7 days of immersion and thereafter a decrease with immersion time. There was a decrease in the weight percentage of the P and Ca with an increase in the weight percentage of the O after immersion in the SBF for 56 days for both samples. After 56 days of immersion, the flat disks samples were found to have aluminium, silicone, and chlorine. The weight percentage of P and Ca decreased with immersion time due to nucleation and precipitation taking place on the surface of the coating while the O increased as a result.

XRD results revealed that the cylinder samples have HAp peaks with higher intensity as compared to the peaks of the flat disks XRD patterns. However, XRD quantitative phase analysis for both sample geometries showed HAp being the dominant phase. The HAp for the cylinder geometry substrates increased with immersion for 7 days and thereafter stabilized whereas for the flat disk substrates, it increased after 7 days of immersion and thereafter decreased slightly with immersion time eventually both reaching the same weight percentage. The CaO thermal product disappears after 7 days of immersion for both geometries and the TCP and TTCP decrease after 7 days, which was due to the thermal products dissolving in the immersion liquid. Thereafter the TTCP decreases with immersion time for the cylinder samples and increases a little bit for the flat disks. The TCP starts to increase after 28 days of immersion and continues increasing with immersion time for both sample geometries.

The residual stress investigation revealed that the stress found within the coatings are tensile for both geometry thicknesses. For the coatings deposited on the cylinder samples, the initial average stress after air plasma spraying was 54.35 MPa. This exceeds the ultimate tensile stress (UTS), 38.0 - 48.0 MPa, of the material hence the cracks observed on the coating surface. After 7 days of immersion the stress decreased to 51.38 MPa and then to 42.07 MPa with immersion for 28 days. The stress thereafter

relaxed to 35.57 MPa after 56 days of immersion in the SBF. The residual stress in the coatings deposited on the flat disk samples was 37.72 MPa after air plasma spraying. Thereafter it increased to 40.10 MPa upon immersion for 7 days in SBF where it exceeds the UTS. It then appears to decrease with immersion time to 30.79 MPa after 28 days and thereafter decreases only slightly to 29.57 MPa. Eventually after 56 days of immersion, the average of the normal stresses for both substrates reaches the same amount within error margins. The shear components, $\sigma_{ij's}$ are negligible, not exceeding 12 MPa and was, therefore, not considered.

The microstructure of the air plasma sprayed hydroxyapatite coatings deposited showed the surface becoming relatively more crystalline with immersion in the SBF. In both substrate geometries a precipitate layer begins to nucleate on the surface with immersion in the SBF.

HAp appears to be the dominant phase in both substrate geometries after air plasma spraying with thermal product TTCP being the dominant thermal product. However, HAp peaks appeared intense for cylinder substrate XRD patterns as compared to that of the flat disk substrates. CaO disappears after immersion in the SBF for both geometries.

The as-sprayed residual stresses in the coatings deposited on the cylinder substrates were higher than the stress in the coatings deposited on the flat disk substrates. Therefore, plasma spraying causes large stresses on thicker substrates therefore possibly compromising the stability of these coatings. The stresses for the cylinder substrates exceeded the UTS range after air plasma spraying and thereafter decreased. The stress after 7 days of immersion increased for the flat disks but decreased for the cylinder sample as the stress had already exceeded the UTS. After immersion for 28 days both samples had a decrease in the stress and both samples continued to show a decrease in the stress with further immersion for 56 days.

The normal stresses appear homogenous, within the error margins, throughout the surface of the coatings. There are some outliers present however this technique proved reliable to produce relatively homogenous coatings. The normal stresses of the samples collected from the same batch also appear to agree, within the error margin, which suggests that this technique is reliable in coating several substrates with a reasonable degree of reproducibility.

The stress observed after air plasma spraying the 25mm thick (cylinder) substrate was higher than the stress observed on the 5mm thick (flat) disk substrates. Therefore, the thicker the substrate the larger the residual stresses present within the sample. This is undesirable as it would put the reliability of the sample stability at risk for load bearing applications. However, after immersion within the SBF for 56 days, the two samples were observed to have the equal residual stresses, within error margins. It therefore may seem that air plasma spraying would not be suitable for coating of thicker substrates however this problem could be solved by increasing the temperature of the thicker substrate prior to deposition.

7.2 Future work

The following work will be focused on:

- Depth resolved investigation of phase composition, crystallinity and residual stresses employing high energy synchrotron radiation or layer removal method in conjunction with XRD to fully appreciate the effect of substrate thickness.
- Investigating coatings deposited on intermediate and additional substrate thicknesses.
- Additional intermediate immersion periods within first 10 days given that significant changes took place during this period.

Appendix A: Stress results

Table A1: *Residual stress on the surface of the coating deposited on cylinder substrates for various immersion periods.*

Immersion period	**Stress (MPa)**	
	σ_{11}	**σ_{22}**
As-sprayed	55.70 ± 11.09	56.59 ± 10.94
	56.19 ± 10.59	45.55 ± 10.44
	59.32 ± 11.08	65.38 ± 10.92
	53.28 ± 10.51	42.21 ± 10.36
	55.17 ± 10.41	54.91 ± 10.26
	61.54 ± 10.40	55.30 ± 10.26
	50.74 ± 10.27	59.12 ± 10.13
	49.73 ± 10.22	50.24 ± 10.08
	53.69 ± 10.43	62.11 ± 10.29
	45.03 ± 10.21	55.11 ± 10.08
Average of data points	54.04 ± 1.51	54.65 ± 2.24
Average of normal stresses	54.35 ± 0.31	
7 days	54.06 ± 10.34	42.96 ± 10.19
	63.45 ± 9.59	63.88 ± 11.19
	54.68 ± 10.40	32.48 ± 12.16
	51.93 ± 9.69	62.32 ± 11.32
	39.56 ± 9.00	40.72 ± 10.52
	57.87 ± 10.28	51.20 ± 12.01

	68.30 ± 9.74	63.85 ± 11.37
	57.13 ± 9.18	27.62 ± 10.73
	52.01 ± 9.25	58.67 ± 10.81
	39.23 ± 8.87	45.68 ± 10.37
Average of data points	53.82 ± 2.89	48.94 ± 4.17
Average of normal stresses	51.38 ± 2.44	
	45.98 ± 8.07	44.64 ± 9.44
	52.18 ± 8.81	39.13 ± 10.30
	52.34 ± 9.34	33.42 ± 10.92
28 days	41.39 ± 9.93	42.93 ± 9.79
	38.98 ± 8.35	33.44 ± 9.77
	50.06 ± 10.52	52.17 ± 12.30
	45.81 ± 10.52	42.38 ± 10.37
	36.15 ± 8.70	31.92 ± 10.17
	44.13 ± 9.17	38.68 ± 10.73
	34.68 ± 8.80	40.95 ± 10.29
Average of data points	44.17 ± 2.00	39.97 ± 1.94
Average of normal stresses	42.07 ± 2.10	
	40.18 ± 7.41	23.99 ± 8.69
	42.31 ± 7.51	30.97 ± 8.79
	51.48 ± 8.63	18.93 ± 10.10
	19.91 ± 8.32	27.77 ± 9.74
	39.64 ± 8.72	38.11 ± 10.20
56 days	34.89 ± 9.92	31.99 ± 11.61

	41.74 ± 8.33	37.70 ± 9.74
	50.27 ± 8.32	32.79 ± 9.74
	39.11 ± 8.19	34.29 ± 9.59
	31.99 ± 8.10	43.30 ± 9.48
Average of data points	39.15 ± 2.85	31.98 ± 2.25
Average of normal stresses	35.57 ± 3.59	

Table A2: *Residual stress on the surface of the coating deposited on flat disk substrates for various immersion periods.*

Immersion period	**Stress (MPa)**	
	σ_{11}	**σ_{22}**
As-sprayed	35.13 ± 9.63	31.07 ± 9.50
	38.24 ± 9.55	41.21 ± 9.41
	39.44 ± 9.47	37.56 ± 9.33
	31.94 ± 7.96	39.30 ± 7.85
	37.02 ± 7.98	48.88 ± 7.87
	43.12 ± 7.94	39.79 ± 7.82
	37.02 ± 12.55	29.44 ± 12.37
	32.34 ± 7.70	42.07 ± 7.59
Average of data points	36.78 ± 1.31	38.66 ± 2.19
Average of normal stresses	37.72 ± 0.94	
	35.40 ± 9.62	30.85 ± 9.48
	61.04 ± 9.08	50.97 ± 10.23
	53.59 ± 8.81	24.95 ± 9.93

7 days	31.37 ± 9.73	37.09 ± 9.60
	41.05 ± 8.25	33.81 ± 9.65
	37.86 ± 9.43	28.40 ± 9.30
	56.52 ± 8.91	47.73 ± 10.42
	46.27 ± 8.43	21.50 ± 9.86
	37.66 ± 8.58	51.83 ± 10.03
	35.82 ± 8.29	38.19 ± 9.70
Average of data points	43.66 ± 3.21	36.53 ± 3.39
Average of normal stresses	40.10 ± 3.57	
28 days	31.91 ± 9.37	31.94 ± 9.24
	32.18 ± 9.57	30.46 ± 9.44
	31.11 ± 9.41	20.71 ± 9.29
	34.32 ± 9.73	32.49 ± 9.60
	25.81 ± 9.24	28.75 ± 9.12
	25.80 ± 9.61	28.26 ± 9.49
	33.81 ± 9.31	35.22 ± 9.19
	30.70 ± 9.26	25.36 ± 9.14
	32.52 ± 9.68	32.89 ± 9.55
	18.05 ± 9.33	19.02 ± 9.22
Average of data points	30.91 ± 1.04	30.67 ± 1.47
Average of normal stresses	30.79 ± 0.12	
	38.22 ± 9.41	26.93 ± 9.29
	30.80 ± 9.95	34.19 ± 9.38
	33.48 ± 9.15	27.43 ± 9.03

56 days	23.57 ± 9.06	21.87 ± 7.67
	57.17 ± 10.71	33.31 ± 9.71
Average of data points	31.52 ± 3.06	27.61 ± 2.53
Average of normal stresses	29.57 ± 1.96	